

High- E_T dijet photoproduction at HERA

ZEUS Collaboration

Abstract

The cross section for high- E_T dijet production in photoproduction has been measured with the ZEUS detector at HERA using an integrated luminosity of 81.8 pb^{-1} . The events were required to have a virtuality of the incoming photon, Q^2 , of less than 1 GeV^2 and a photon-proton center-of-mass energy in the range $142 < W_{\gamma p} < 293 \text{ GeV}$. Events were selected if at least two jets satisfied the transverse-energy requirements of $E_T^{\text{jet}1} > 20 \text{ GeV}$ and $E_T^{\text{jet}2} > 15 \text{ GeV}$ and pseudorapidity (with respect to the proton beam direction) requirements of $-1 < \eta^{\text{jet}1,2} < 3$, with at least one of the jets satisfying $-1 < \eta^{\text{jet}} < 2.5$. The measurements show sensitivity to the parton distributions in the photon and proton and to effects beyond next-to-leading order in QCD. Hence these data can be used to constrain further the parton densities in the proton and photon.

The ZEUS Collaboration

S. Chekanov¹, M. Derrick, S. Magill, B. Musgrave, D. Nicholass², J. Repond, R. Yoshida
*Argonne National Laboratory, Argonne, Illinois 60439-4815, USA*ⁿ

M.C.K. Mattingly

Andrews University, Berrien Springs, Michigan 49104-0380, USA

M. Jechow, N. Pavel[†], A.G. Yagües Molina

Institut für Physik der Humboldt-Universität zu Berlin, Berlin, Germany

S. Antonelli, P. Antonioli, G. Bari, M. Basile, L. Bellagamba, M. Bindi, D. Boscherini,
A. Bruni, G. Bruni, L. Cifarelli, F. Cindolo, A. Contin, M. Corradi, S. De Pasquale,
G. Iacobucci, A. Margotti, R. Nania, A. Polini, G. Sartorelli, A. Zichichi

University and INFN Bologna, Bologna, Italy^e

D. Bartsch, I. Brock, S. Goers³, H. Hartmann, E. Hilger, H.-P. Jakob, M. Jüngst, O.M. Kind⁴,
A.E. Nuncio-Quiroz, E. Paul⁵, R. Renner⁶, U. Samson, V. Schönberg, R. Shehzadi, M. Wlasenko
Physikalisches Institut der Universität Bonn, Bonn, Germany^b

N.H. Brook, G.P. Heath, J.D. Morris

H.H. Wills Physics Laboratory, University of Bristol, Bristol, United Kingdom^m

M. Capua, S. Fazio, A. Mastroberardino, M. Schioppa, G. Susinno, E. Tassi

Calabria University, Physics Department and INFN, Cosenza, Italy^e

J.Y. Kim⁷, K.J. Ma⁸

Chonnam National University, Kwangju, South Korea^g

Z.A. Ibrahim, B. Kamaluddin, W.A.T. Wan Abdullah

Jabatan Fizik, Universiti Malaya, 50603 Kuala Lumpur, Malaysia^r

Y. Ning, Z. Ren, F. Sciulli

Nevis Laboratories, Columbia University, Irvington on Hudson, New York 10027^o

J. Chwastowski, A. Eskreys, J. Figiel, A. Galas, M. Gil, K. Olkiewicz, P. Stopa, L. Zawiejski

*The Henryk Niewodniczanski Institute of Nuclear Physics, Polish Academy of Sciences, Cracow, Poland*ⁱ

L. Adamczyk, T. Bołd, I. Grabowska-Bołd, D. Kisielewska, J. Łukasik, M. Przybycień,
L. Suszycki

Faculty of Physics and Applied Computer Science, AGH-University of Science and Technology, Cracow, Poland^p

A. Kotański⁹, W. Słomiński¹⁰

Department of Physics, Jagellonian University, Cracow, Poland

V. Adler¹¹, U. Behrens, I. Bloch, C. Blohm, A. Bonato, K. Borras, R. Ciesielski, N. Coppola, A. Dossanov, V. Drugakov, J. Fourletova, A. Geiser, D. Gladkov, P. Göttlicher¹², J. Grebenyuk, I. Gregor, T. Haas, W. Hain, C. Horn¹³, A. Hüttmann, B. Kahle, I.I. Katkov, U. Klein¹⁴, U. Kötz, H. Kowalski, E. Lobodzinska, B. Löhr, R. Mankel, I.-A. Melzer-Pellmann, S. Miglioranza, A. Montanari, T. Namsoo, D. Notz, L. Rinaldi, P. Roloff, I. Rubinsky, R. Santamarta, U. Schneekloth, A. Spiridonov¹⁵, H. Stadie, D. Szuba¹⁶, J. Szuba¹⁷, T. Theedt, G. Wolf, K. Wrona, C. Youngman, W. Zeuner
Deutsches Elektronen-Synchrotron DESY, Hamburg, Germany

W. Lohmann, S. Schlenstedt
Deutsches Elektronen-Synchrotron DESY, Zeuthen, Germany

G. Barbagli, E. Gallo, P. G. Pelfer
University and INFN, Florence, Italy^e

A. Bamberger, D. Dobur, F. Karstens, N.N. Vlasov¹⁸
Fakultät für Physik der Universität Freiburg i.Br., Freiburg i.Br., Germany^b

P.J. Bussey, A.T. Doyle, W. Dunne, J. Ferrando, M. Forrest, D.H. Saxon, I.O. Skillicorn
Department of Physics and Astronomy, University of Glasgow, Glasgow, United Kingdom^m

I. Gialas¹⁹, K. Papageorgiu
Department of Engineering in Management and Finance, Univ. of Aegean, Greece

T. Gosau, U. Holm, R. Klanner, E. Lohrmann, H. Perrey, H. Salehi, P. Schleper, T. Schörner-Sadenius, J. Sztuk, K. Wichmann, K. Wick
Hamburg University, Institute of Exp. Physics, Hamburg, Germany^b

C. Foudas, C. Fry, K.R. Long, A.D. Tapper
Imperial College London, High Energy Nuclear Physics Group, London, United Kingdom^m

M. Kataoka²⁰, T. Matsumoto, K. Nagano, K. Tokushuku²¹, S. Yamada, Y. Yamazaki
Institute of Particle and Nuclear Studies, KEK, Tsukuba, Japan^f

A.N. Barakbaev, E.G. Boos, N.S. Pokrovskiy, B.O. Zhautykov
Institute of Physics and Technology of Ministry of Education and Science of Kazakhstan, Almaty, Kazakhstan

V. Aushev¹
Institute for Nuclear Research, National Academy of Sciences, Kiev and Kiev National University, Kiev, Ukraine

D. Son
Kyungpook National University, Center for High Energy Physics, Daegu, South Korea^g

J. de Favereau, K. Piotrkowski

Institut de Physique Nucléaire, Université Catholique de Louvain, Louvain-la-Neuve, Belgium^g

F. Barreiro, C. Glasman²², M. Jimenez, L. Labarga, J. del Peso, E. Ron, M. Soares, J. Terrón, M. Zambrana

Departamento de Física Teórica, Universidad Autónoma de Madrid, Madrid, Spain^l

F. Corriveau, C. Liu, R. Walsh, C. Zhou

Department of Physics, McGill University, Montréal, Québec, Canada H3A 2T8^a

T. Tsurugai

Meiji Gakuin University, Faculty of General Education, Yokohama, Japan^f

A. Antonov, B.A. Dolgoshein, V. Sosnovtsev, A. Stifutkin, S. Suchkov

Moscow Engineering Physics Institute, Moscow, Russia^j

R.K. Dementiev, P.F. Ermolov, L.K. Gladilin, L.A. Khein, I.A. Korzhavina, V.A. Kuzmin, B.B. Levchenko²³, O.Yu. Lukina, A.S. Proskuryakov, L.M. Shcheglova, D.S. Zotkin, S.A. Zotkin

Moscow State University, Institute of Nuclear Physics, Moscow, Russia^k

I. Abt, C. Büttner, A. Caldwell, D. Kollar, W.B. Schmidke, J. Sutiak

Max-Planck-Institut für Physik, München, Germany

G. Grigorescu, A. Keramidas, E. Koffeman, P. Kooijman, A. Pellegrino, H. Tiecke, M. Vázquez²⁰, L. Wiggers

NIKHEF and University of Amsterdam, Amsterdam, Netherlands^h

N. Brümmer, B. Bylsma, L.S. Durkin, A. Lee, T.Y. Ling

Physics Department, Ohio State University, Columbus, Ohio 43210ⁿ

P.D. Allfrey, M.A. Bell, A.M. Cooper-Sarkar, A. Cottrell, R.C.E. Devenish, B. Foster, K. Korcsak-Gorzo, S. Patel, V. Roberfroid²⁴, A. Robertson, P.B. Straub, C. Uribe-Estrada, R. Walczak

Department of Physics, University of Oxford, Oxford United Kingdom^m

P. Bellan, A. Bertolin, R. Brugnera, R. Carlin, F. Dal Corso, S. Dusini, A. Garfagnini, S. Limentani, A. Longhin, L. Stanco, M. Turcato

Dipartimento di Fisica dell'Università and INFN, Padova, Italy^e

B.Y. Oh, A. Raval, J. Ukleja²⁵, J.J. Whitmore²⁶

Department of Physics, Pennsylvania State University, University Park, Pennsylvania 16802^o

Y. Iga

Polytechnic University, Sagamihara, Japan^f

G. D'Agostini, G. Marini, A. Nigro
Dipartimento di Fisica, Università 'La Sapienza' and INFN, Rome, Italy^e

J.E. Cole, J.C. Hart
Rutherford Appleton Laboratory, Chilton, Didcot, Oxon, United Kingdom^m

H. Abramowicz²⁷, A. Gabareen, R. Ingbir, S. Kananov, A. Levy
Raymond and Beverly Sackler Faculty of Exact Sciences, School of Physics, Tel-Aviv University, Tel-Aviv, Israel^d

M. Kuze, J. Maeda
Department of Physics, Tokyo Institute of Technology, Tokyo, Japan^f

R. Hori, S. Kagawa²⁸, N. Okazaki, S. Shimizu, T. Tawara
Department of Physics, University of Tokyo, Tokyo, Japan^f

R. Hamatsu, H. Kaji²⁹, S. Kitamura³⁰, O. Ota, Y.D. Ri
Tokyo Metropolitan University, Department of Physics, Tokyo, Japan^f

M.I. Ferrero, V. Monaco, R. Sacchi, A. Solano
Università di Torino and INFN, Torino, Italy^e

M. Arneodo, M. Ruspa
Università del Piemonte Orientale, Novara, and INFN, Torino, Italy^e

S. Fourletov, J.F. Martin
Department of Physics, University of Toronto, Toronto, Ontario, Canada M5S 1A7^a

S.K. Boutle¹⁹, J.M. Butterworth, C. Gwenlan³¹, T.W. Jones, J.H. Loizides, M.R. Sutton³¹,
C. Targett-Adams, M. Wing
Physics and Astronomy Department, University College London, London, United Kingdom^m

B. Brzozowska, J. Ciborowski³², G. Grzelak, P. Kulinski, P. Luźniak³³, J. Malka³³, R.J. Nowak,
J.M. Pawlak, T. Tymieniecka, A. Ukleja, A.F. Żarnecki
Warsaw University, Institute of Experimental Physics, Warsaw, Poland

M. Adamus, P. Plucinski³⁴
Institute for Nuclear Studies, Warsaw, Poland

Y. Eisenberg, I. Giller, D. Hochman, U. Karshon, M. Rosin
Department of Particle Physics, Weizmann Institute, Rehovot, Israel^c

E. Brownson, T. Danielson, A. Everett, D. Kçira, D.D. Reeder⁵, P. Ryan, A.A. Savin,
W.H. Smith, H. Wolfe
*Department of Physics, University of Wisconsin, Madison, Wisconsin 53706, USA*ⁿ

S. Bhadra, C.D. Catterall, Y. Cui, G. Hartner, S. Menary, U. Noor, J. Standage, J. Whyte
Department of Physics, York University, Ontario, Canada M3J 1P3^a

- ¹ supported by DESY, Germany
- ² also affiliated with University College London, UK
- ³ now with TÜV Nord, Germany
- ⁴ now at Humboldt University, Berlin, Germany
- ⁵ retired
- ⁶ self-employed
- ⁷ supported by Chonnam National University in 2005
- ⁸ supported by a scholarship of the World Laboratory Björn Wiik Research Project
- ⁹ supported by the research grant no. 1 P03B 04529 (2005-2008)
- ¹⁰ This work was supported in part by the Marie Curie Actions Transfer of Knowledge project COCOS (contract MTKD-CT-2004-517186)
- ¹¹ now at Univ. Libre de Bruxelles, Belgium
- ¹² now at DESY group FEB, Hamburg, Germany
- ¹³ now at Stanford Linear Accelerator Center, Stanford, USA
- ¹⁴ now at University of Liverpool, UK
- ¹⁵ also at Institut of Theoretical and Experimental Physics, Moscow, Russia
- ¹⁶ also at INP, Cracow, Poland
- ¹⁷ on leave of absence from FPACS, AGH-UST, Cracow, Poland
- ¹⁸ partly supported by Moscow State University, Russia
- ¹⁹ also affiliated with DESY
- ²⁰ now at CERN, Geneva, Switzerland
- ²¹ also at University of Tokyo, Japan
- ²² Ramón y Cajal Fellow
- ²³ partly supported by Russian Foundation for Basic Research grant no. 05-02-39028-NSFC-a
- ²⁴ EU Marie Curie Fellow
- ²⁵ partially supported by Warsaw University, Poland
- ²⁶ This material was based on work supported by the National Science Foundation, while working at the Foundation.
- ²⁷ also at Max Planck Institute, Munich, Germany, Alexander von Humboldt Research Award
- ²⁸ now at KEK, Tsukuba, Japan
- ²⁹ now at Nagoya University, Japan
- ³⁰ Department of Radiological Science
- ³¹ PPARC Advanced fellow
- ³² also at Łódź University, Poland
- ³³ Łódź University, Poland
- ³⁴ supported by the Polish Ministry for Education and Science grant no. 1 P03B 14129
- † deceased

- a* supported by the Natural Sciences and Engineering Research Council of Canada (NSERC)
- b* supported by the German Federal Ministry for Education and Research (BMBF), under contract numbers HZ1GUA 2, HZ1GUB 0, HZ1PDA 5, HZ1VFA 5
- c* supported in part by the MINERVA Gesellschaft für Forschung GmbH, the Israel Science Foundation (grant no. 293/02-11.2) and the U.S.-Israel Binational Science Foundation
- d* supported by the German-Israeli Foundation and the Israel Science Foundation
- e* supported by the Italian National Institute for Nuclear Physics (INFN)
- f* supported by the Japanese Ministry of Education, Culture, Sports, Science and Technology (MEXT) and its grants for Scientific Research
- g* supported by the Korean Ministry of Education and Korea Science and Engineering Foundation
- h* supported by the Netherlands Foundation for Research on Matter (FOM)
- i* supported by the Polish State Committee for Scientific Research, grant no. 620/E-77/SPB/DESY/P-03/DZ 117/2003-2005 and grant no. 1P03B07427/2004-2006
- j* partially supported by the German Federal Ministry for Education and Research (BMBF)
- k* supported by RF Presidential grant N 8122.2006.2 for the leading scientific schools and by the Russian Ministry of Education and Science through its grant Research on High Energy Physics
- l* supported by the Spanish Ministry of Education and Science through funds provided by CICYT
- m* supported by the Particle Physics and Astronomy Research Council, UK
- n* supported by the US Department of Energy
- o* supported by the US National Science Foundation. Any opinion, findings and conclusions or recommendations expressed in this material are those of the authors and do not necessarily reflect the views of the National Science Foundation.
- p* supported by the Polish Ministry of Science and Higher Education as a scientific project (2006-2008)
- q* supported by FNRS and its associated funds (IISN and FRiA) and by an Inter-University Attraction Poles Programme subsidised by the Belgian Federal Science Policy Office
- r* supported by the Malaysian Ministry of Science, Technology and Innovation/Akademi Sains Malaysia grant SAGA 66-02-03-0048

1 Introduction

In photoproduction at HERA, a quasi-real photon emitted from the incoming positron¹ collides with a parton from the incoming proton. The photoproduction of jets can be classified into two types of processes in leading-order (LO) Quantum Chromodynamics (QCD). In direct processes, the photon participates in the hard scatter via either boson-gluon fusion (see Fig. 1(a)) or QCD Compton scattering. The second class, resolved processes (see Fig. 1(b)), involves the photon acting as a source of quarks and gluons, with only a fraction of its momentum, x_γ , participating in the hard scatter. Measurements of jet cross sections in photoproduction [1–6] are sensitive to the structure of both the proton and the photon and thus provide input to global fits to determine their parton densities.

There are three objectives of the measurement reported in this paper. Firstly, the analysis was designed to provide constraints on the parton density functions (PDFs) of the photon. Over the last two years there has been active research in the area of fitting photon PDFs and a number of new parameterizations have become available [7–9]. In two of these [7, 8], fits were performed exclusively to photon structure function, F_2^γ , data; the other [9] also considered data from a previous dijet photoproduction analysis published by the ZEUS collaboration [4]. It is the purpose of this analysis to test the effectiveness of each parameterization at describing HERA photoproduction data. To this end, the present analysis was conducted at higher transverse energy relative to previous publications. It is expected that at these high transverse energies the predictions of next-to-leading-order (NLO) QCD calculations should describe the data well, have smaller uncertainties, and allow a more precise discrimination between the different parameterizations of the photon PDFs. The reduction in statistics associated with moving to higher transverse energies was in part compensated by the factor of two increase in luminosity, for this independent data sample, and the extension to higher pseudorapidity² of the jet compared to the previous analysis [4].

Secondly, the present analysis was designed to provide constraints on the proton PDFs. Global fits to determine the proton PDFs continue to be a very active and important area of research. A common feature of these global fits is a large uncertainty in the gluon PDF for high values of x_p , the fractional momentum at which partons inside the proton

¹ In the following, the term “positron” denotes generically both the electron (e^-) and positron (e^+). Unless explicitly stated, positron will be the term used to describe both particles.

² The ZEUS coordinate system is a right-handed Cartesian system, with the Z axis pointing in the proton beam direction, referred to as the “forward direction”, and the X axis pointing left towards the center of HERA. The coordinate origin is at the nominal interaction point. The pseudorapidity is defined as $\eta = -\ln\left(\tan\frac{\theta}{2}\right)$, where the polar angle, θ , is measured with respect to the proton beam direction.

are probed. At such high values ($x_p \gtrsim 0.1$), the gluon PDF is poorly constrained and so attempts were made for the present investigation to measure cross sections which show particular sensitivity to these uncertainties. Recently, the ZEUS collaboration included jet data into fits for the proton PDFs [10].

Finally, the difference in azimuthal angle of two jets was considered, as in previous measurements of charm and prompt photon photoproduction [11, 12]. In LO QCD, the cross section as a function of the azimuthal difference would simply be a delta function located at π radians. However, the presence of higher-order effects leads to extra jets in the final state and in values less than π radians. The cross section is therefore directly sensitive to higher-order topologies and provides a test of NLO QCD and of Monte Carlo (MC) models with different implementations of parton-cascade algorithms. The data for charm photoproduction [11] demonstrated the inadequacy of NLO QCD, particularly when the azimuthal angle difference was significantly different from π and for a sample of events enriched in resolved-photon processes. To investigate this inadequacy in a more inclusive way and with higher precision, such distributions were also measured.

2 Definition of the cross section and variables

Within the framework of perturbative QCD, the dijet positron-proton cross section, $d\sigma_{ep}$, can be written as a convolution of the proton PDFs, f_p , and photon PDFs, f_γ , with the partonic hard cross section, $d\hat{\sigma}_{ab}$, as

$$d\sigma_{ep} = \sum_{ab} \int dy f_{\gamma/e}(y) \int \int dx_p dx_\gamma f_p(x_p, \mu_F^2) f_\gamma(x_\gamma, \mu_F^2) d\hat{\sigma}_{ab}(x_p, x_\gamma, \mu_R^2), \quad (1)$$

where $y = E_\gamma/E_e$ is the longitudinal momentum fraction of the almost-real photon emitted by the positron and the function $f_{\gamma/e}$ is the flux of photons from the positron. The equation is a sum over all possible partons, a and b . In the case of the direct cross section, the photon PDF is replaced by a delta function at $x_\gamma = 1$. The scales of the process are the renormalization, μ_R , and factorization scales, μ_F .

To probe the structure of the photon, it is desirable to measure cross sections as functions of variables that are sensitive to the incoming parton momentum spectrum, such as the momentum fraction, x_γ , at which partons inside the photon are probed. Since x_γ is not directly measurable, it is necessary to define [1] an observable, x_γ^{obs} , which is the fraction of the photon momentum participating in the production of the two highest transverse-energy jets (and is equal to x_γ for partons in LO QCD), as:

$$x_\gamma^{\text{obs}} = \frac{E_T^{\text{jet1}} e^{-\eta^{\text{jet1}}} + E_T^{\text{jet2}} e^{-\eta^{\text{jet2}}}}{2yE_e}, \quad (2)$$

where E_e is the incident positron energy, E_T^{jet1} and E_T^{jet2} are the transverse energies and η^{jet1} and η^{jet2} the pseudorapidities of the two jets in the laboratory frame ($E_T^{\text{jet1}} > E_T^{\text{jet2}}$). At LO (see Fig. 1), direct processes have $x_\gamma^{\text{obs}} = 1$, while resolved processes have $x_\gamma^{\text{obs}} < 1$.

For the proton, the observable x_p^{obs} is similarly defined [1] as

$$x_p^{\text{obs}} = \frac{E_T^{\text{jet1}} e^{\eta^{\text{jet1}}} + E_T^{\text{jet2}} e^{\eta^{\text{jet2}}}}{2E_p}, \quad (3)$$

where E_p is the incident proton energy. This observable is the fraction of the proton momentum participating in the production of the two highest-energy jets (and is equal to x_p for partons in LO QCD).

Cross sections are presented as functions of x_γ^{obs} , x_p^{obs} , \bar{E}_T , E_T^{jet1} , $\bar{\eta}$ and $|\Delta\phi^{\text{jj}}|$. The mean transverse energy of the two jets, \bar{E}_T , is given by

$$\bar{E}_T = \frac{E_T^{\text{jet1}} + E_T^{\text{jet2}}}{2}. \quad (4)$$

Similarly, the mean pseudorapidity of the two jets, $\bar{\eta}$, is given by

$$\bar{\eta} = \frac{\eta^{\text{jet1}} + \eta^{\text{jet2}}}{2}. \quad (5)$$

The absolute difference in azimuthal angle of the two jets, ϕ^{jet1} and ϕ^{jet2} , is given by

$$|\Delta\phi^{\text{jj}}| = |\phi^{\text{jet1}} - \phi^{\text{jet2}}|. \quad (6)$$

The kinematic region for this study is defined as $Q^2 < 1 \text{ GeV}^2$, where $Q^2 = 2E_e E'_e (1 + \cos\theta_e)$ and E'_e and θ_e are the energy and angle, respectively, of the scattered positron. The photon-proton center-of-mass energy, $W_{\gamma p} = \sqrt{4yE_e E_p}$, is required to be in the range 142 GeV to 293 GeV. Each event is required to have at least two jets reconstructed with the k_T cluster algorithm [13] in its longitudinally invariant inclusive mode [14], with at least one jet having transverse energy greater than 20 GeV and another greater than 15 GeV. The jets are required to satisfy $-1 < \eta^{\text{jet1,2}} < 3$ with at least one jet lying in the range between -1 and 2.5 . The upper bound of 3 units represents an extension of the pseudorapidity range by 0.6 units in the forward direction over the previous analysis [4], thereby increasing the sensitivity of the measurement to low- x_γ and high- x_p processes. The cross sections for all distributions have been determined for regions enriched in direct-

and resolved-photon processes by requiring x_γ^{obs} to be greater than 0.75 or less than 0.75, respectively.

One of the goals of the present investigation is to provide data that constrain the gluon PDF in the proton, which exhibits large uncertainties at values of $x_p \gtrsim 0.1$. A study was performed [15] by considering the x_p^{obs} cross section in different kinematic regions, varying the cuts on the jet transverse energies and pseudorapidities as well as on x_γ^{obs} . This allowed the determination of kinematic regions in which the cross section was large enough to be measured and in which the uncertainties on the cross section that arise due to those of the gluon PDF were largest. These cross sections will be referred to as “optimized” cross sections and are those which have the largest uncertainty from the gluon PDF; in total eight cross sections were measured (four direct enriched and four resolved enriched). The PDF sets chosen to conduct the optimization study were the ZEUS-S [16] and ZEUS-JETS [10] PDF sets. The kinematic regions of the cross sections are defined in Table 1, where the $W_{\gamma p}$ and Q^2 requirements are as above.

3 Experimental conditions

The data were collected during the 1998-2000 running periods, where HERA operated with protons of energy $E_p = 920$ GeV and electrons or positrons of energy $E_e = 27.5$ GeV. During 1998 and the first half of 1999, a sample of electron data corresponding to an integrated luminosity of 16.7 ± 0.3 pb⁻¹ was collected. The remaining data up to the year 2000 were taken using positrons and correspond to an integrated luminosity of 65.1 ± 1.5 pb⁻¹. The results presented here are therefore based on a total integrated luminosity of 81.8 ± 1.8 pb⁻¹. A detailed description of the ZEUS detector can be found elsewhere [17, 18]. A brief outline of the components that are most relevant for this analysis is given below.

Charged particles are tracked in the central tracking detector (CTD) [19], which operates in a magnetic field of 1.43 T provided by a thin superconducting coil. The CTD consists of 72 cylindrical drift chamber layers, organized in 9 superlayers covering the polar-angle region $15^\circ < \theta < 164^\circ$. The transverse-momentum resolution for full-length tracks is $\sigma(p_T)/p_T = 0.0058p_T \oplus 0.0065 \oplus 0.0014/p_T$, with p_T in GeV.

The high-resolution uranium-scintillator calorimeter (CAL) [20] consists of three parts: the forward (FCAL), the barrel (BCAL) and the rear (RCAL) calorimeters. Each part is subdivided transversely into towers and longitudinally into one electromagnetic section (EMC) and either one (in RCAL) or two (in BCAL and FCAL) hadronic sections (HAC). The smallest subdivision of the calorimeter is called a cell. The CAL energy resolutions, as measured under test-beam conditions, are $\sigma(E)/E = 0.18/\sqrt{E}$ for electrons

and $\sigma(E)/E = 0.35/\sqrt{E}$ for hadrons, with E in GeV.

The luminosity was measured from the rate of the bremsstrahlung process $ep \rightarrow e\gamma p$, where the photon was measured in a lead-scintillator calorimeter [21] placed in the HERA tunnel at $Z = -107$ m.

4 Monte Carlo models

The acceptance and the effects of detector response were determined using samples of simulated events. The programs HERWIG 6.505 [22] and PYTHIA 6.221 [23], which implement the leading-order matrix elements, followed by parton showers and hadronization, were used. The HERWIG and PYTHIA generators differ in the details of the implementation of the leading-logarithmic parton-shower models and hence are also compared to the measured cross-section $d\sigma/d|\Delta\phi^{\text{jj}}|$. The MC programs also use different hadronization models: HERWIG uses the cluster model [24] and PYTHIA uses the Lund string model [25]. Direct and resolved events were generated separately. For the purposes of correction, the relative contribution of direct and resolved events was fitted to the data. For all generated events, the ZEUS detector response was simulated in detail using a program based on GEANT 3.13 [26].

For both MC programs, the CTEQ5L [27] and GRV-LO [28] proton and photon PDFs, respectively, were used. The p_T^{min} for the outgoing partons from the hard scatter was set to 4 GeV. For the generation of resolved photon events, the default multiparton interaction models [29,30] were used. A comparably reasonable description of the raw data kinematic distributions was observed with both HERWIG and PYTHIA MC simulations.

5 NLO QCD calculations

The calculation for jet photoproduction used is that of Frixione and Ridolfi [31,32], which employs the subtraction method [33] for dealing with the collinear and infra-red divergencies. The number of flavors was set to 5 and the renormalization and factorization scales were both set to $\langle E_T^{\text{parton}} \rangle$, which is half the sum of the transverse energies of the final-state partons. The parton densities in the proton were parameterized using CTEQ5M1 [27]; the value $\alpha_s(M_Z) = 0.118$ used therein was adopted for the central prediction.

The following parameterizations of the photon PDFs were used: Cornet et al. (CJK) [7], Aurenche et al. (AFG04) [8], Slominski et al. (SAL) [9], Glück et al. (GRV-HO) [28] and a previous set of PDFs from Aurenche et al. (AFG) [34]. The three new PDFs [7–9] use all available data on F_2^γ from the LEP experiments. The data are of higher precision and

cover a wider region of phase space, reaching lower in x_γ and higher in the momentum of the exchanged photon, compared to the data used in the AFG and GRV-HO parameterizations. The parameterization from CJK uses a more careful treatment of heavy quarks, whereas that from SAL also considers previous dijet photoproduction data from ZEUS [4]. The most striking difference between the resulting PDFs is that CJK has a more rapid rise of the gluon density at low x_γ .

The NLO QCD predictions were corrected for hadronization effects using a bin-by-bin procedure according to $d\sigma = d\sigma^{\text{NLO}} \cdot C_{\text{had}}$, where $d\sigma^{\text{NLO}}$ is the cross section for partons in the final state of the NLO calculation. The hadronization correction factor, C_{had} , was defined as the ratio of the dijet cross sections after and before the hadronization process, $C_{\text{had}} = d\sigma_{\text{MC}}^{\text{Hadrons}}/d\sigma_{\text{MC}}^{\text{Partons}}$. The value of C_{had} was taken as the mean of the ratios obtained using the HERWIG and PYTHIA predictions. The hadronization correction was generally below 10% in each bin.

Several sources of theoretical uncertainty were investigated, which are given below with their typical size,

- the renormalization scale was changed to $2^{\pm 0.5} \cdot \langle E_T^{\text{parton}} \rangle$ [10]. This led to an uncertainty of $\mp(10 - 20)\%$;
- the factorization scale was changed to $2^{\pm 0.5} \cdot \langle E_T^{\text{parton}} \rangle$ [10]. This led to an uncertainty of $\pm(5 - 10)\%$;
- the value of α_s was changed by ± 0.001 , the uncertainty on the world average [35], by using the CTEQ4 PDFs for $\alpha_s(M_Z) = 0.113, 0.116$ and 0.119 and interpolating accordingly. This led to an uncertainty of about $\pm 2\%$;
- the uncertainty in the hadronization correction was estimated as half the spread between the two MC correction factors. This led to an uncertainty of generally less than $\pm 5\%$.

The above four uncertainties were added in quadrature and are displayed on the figures as the shaded band around the central prediction. The size of these uncertainties is also shown as a function of \bar{E}_T , x_γ^{obs} and x_p^{obs} in Fig. 2. The uncertainty from changing the renormalization scale is dominant. It should be noted that here the renormalization and factorization scales were varied independently by factors of $2^{\pm 0.5}$ and the resulting changes were added in quadrature as in the determination of the ZEUS-JETS PDF [10]. The result of this procedure leads to an uncertainty which is approximately the same as varying both simultaneously by $2^{\pm 1}$ as has been done previously [4].

Other uncertainties which were considered are:

- the uncertainties in determining the proton PDFs were assessed by using the ZEUS-JETS PDF uncertainties propagated from the experimental uncertainties of the fitted

data. This led to an uncertainty of $\pm(5 - 10)\%$;

- the uncertainties in determining the photon PDFs were assessed by using sets from different authors. Differences of generally less than 25% were observed between the AFG, AFG04, SAL and GRV sets. However, the predictions based on CJK were up to 70% higher than those based on the other four.

These uncertainties were not added in quadrature with the others, but examples of their size are given in Fig. 2. Differences between the two photon PDFs, CJK and AFG04, are concentrated at low x_γ^{obs} and low \bar{E}_T ; the low x_γ^{obs} region is most sensitive to the gluon distribution in the photon, which increases more rapidly for CJK as shown in Fig. 3. At lowest x_γ^{obs} , the fraction of the cross section arising from the gluon distribution in the photon is 66% for CJK. The uncertainty on the proton PDF increases with increasing \bar{E}_T and x_p^{obs} and is sometimes, as seen in Fig. 2(c), as large as the other combined uncertainties. The fraction of the cross section arising from the gluon distribution in the proton is about 50% for the lower \bar{E}_T and x_p^{obs} values considered, but decreases to below 20% for high values. However, the uncertainty on the gluon dominates the proton PDF uncertainty in most of the kinematic region investigated.

6 Event selection

A three-level trigger system was used to select events online [2,18,36]. At the third level, a cone algorithm was applied to the CAL cells and jets were reconstructed using the energies and positions of these cells. Events with at least one jet, which satisfied the requirements that the transverse energy exceeded 10 GeV and the pseudorapidity was less than 2.5, were accepted. Dijet events in photoproduction were then selected offline by using the following procedures and cuts designed to remove sources of background:

- to remove background due to proton beam-gas interactions and cosmic-ray showers, the longitudinal position of the reconstructed vertex was required to be in the range $|Z_{\text{vertex}}| < 40$ cm;
- a cut on the ratio of the number of tracks assigned to the primary vertex to the total number of tracks, $N_{\text{trk}}^{\text{vtx}}/N_{\text{trk}} > 0.1$, was also imposed to remove beam-related background, which have values of this ratio typically below 0.1;
- to remove background due to charged current deep inelastic scattering (DIS) and cosmic-ray showers, events were required to have a relative transverse momentum of $p_T/\sqrt{E_T} < 1.5\sqrt{\text{GeV}}$, where p_T and E_T are, respectively, the measured transverse momentum and transverse energy of the event;

- neutral current (NC) DIS events with a scattered positron candidate in the CAL were removed by cutting [1] on the inelasticity, y , which is estimated from the energy, E'_e , and polar angle, θ'_e , of the scattered positron candidate using $y_e = 1 - \frac{E'_e}{2E_e}(1 - \cos\theta'_e)$. Events were rejected if $y_e < 0.7$;
- the requirement $0.15 < y_{\text{JB}} < 0.7$ was imposed, where y_{JB} is the estimator of y measured from the CAL energy deposits according to the Jacquet-Blondel method [37]. The upper cut removed NC DIS events where the positron was not identified and which therefore have a value of y_{JB} close to 1. The lower cut removed proton beam-gas events which typically have a low value of y_{JB} ;
- the k_T -clustering algorithm was applied to the CAL energy deposits. The transverse energies of the jets were corrected [3, 4, 38] in order to compensate for energy losses in inactive material in front of the CAL. Events were selected in which at least two jets were found with $E_T^{\text{jet}1} > 20 \text{ GeV}$, $E_T^{\text{jet}2} > 15 \text{ GeV}$ and $-1 < \eta^{\text{jet}1,2} < 3$, with at least one jet lying in the range between -1 and 2.5 . In this region, the resolution of the jet transverse energy was about 10%.

7 Data correction and systematics

The data were corrected using the MC samples detailed in Section 4 for acceptance and the effects of detector response using the bin-by-bin method, in which the correction factor, as a function of an observable \mathcal{O} in a given bin i , is $C_i(\mathcal{O}) = N_i^{\text{had}}(\mathcal{O})/N_i^{\text{det}}(\mathcal{O})$. The variable $N_i^{\text{had}}(\mathcal{O})$ is the number of events in the simulation passing the kinematic requirements on the hadronic final state described in Section 2 and $N_i^{\text{det}}(\mathcal{O})$ is the number of reconstructed events passing the selection requirements as detailed in Section 6.

The results of a detailed analysis [15, 39] of the possible sources of systematic uncertainty are listed below. Typical values for the systematic uncertainty are quoted for the cross sections as a function of x_γ^{obs} ,

- varying the measured jet energies by $\pm 1\%$ [3, 4, 38] in the simulation, in accordance with the uncertainty in the jet energy scale, gave an uncertainty of $\mp 5\%$;
- the central correction factors were determined using the PYTHIA MC. The HERWIG MC sample was used to assess the model dependency of this correction and gave an uncertainty of $+4\%$, but up to $+12\%$ at lowest x_γ^{obs} ;
- changing the values of the various cuts to remove backgrounds from DIS, cosmic-ray and beam-gas events gave a combined uncertainty of less than $\pm 1\%$;
- varying the fraction of direct processes between 34% and 70% of the total MC sample in order to describe each of the kinematic distributions gave an uncertainty of about

$^{+2\%}$
 $_{-5\%}$;

- changing the proton and photon PDFs to CTEQ4L [27] and WHIT2 [40] respectively in the MC samples gave an uncertainty of about $\pm 1.5\%$ and $\pm 2.5\%$.

The uncertainty in the cross sections due to the jet energy-scale uncertainty is correlated between bins and is therefore displayed separately as a shaded band in Figs. 4–13. All other systematic uncertainties were added in quadrature when displayed in these figures. The choice of MC sample also exhibited some correlation between bins and is hence given separately in Tables 2–20. In addition, an overall normalization uncertainty of 2.2% from the luminosity determination is not included in either the figures or tables.

8 Results

8.1 Dijet differential cross sections

Differential cross-sections $d\sigma/d\bar{E}_T$, $d\sigma/dE_T^{\text{jet1}}$, $d\sigma/d\bar{\eta}$ and $d\sigma/dx_p^{\text{obs}}$ are given in Tables 2–9 and shown in Figs. 4–7 for x_γ^{obs} above and below 0.75. For $x_\gamma^{\text{obs}} > 0.75$, $d\sigma/d\bar{E}_T$ and $d\sigma/dE_T^{\text{jet1}}$ fall by over three orders of magnitude over the \bar{E}_T and E_T^{jet1} ranges measured and the jets are produced up to $\bar{\eta} \sim 2$. For $x_\gamma^{\text{obs}} \leq 0.75$, the slopes of $d\sigma/d\bar{E}_T$ and $d\sigma/dE_T^{\text{jet1}}$ are steeper, with the jets produced further forward in $\bar{\eta}$. It is interesting to note that in both regions of x_γ^{obs} , the data probe high values of x in the proton.

The NLO QCD predictions, corrected for hadronization and using the AFG04 and CJK photon PDFs, are compared to the data. For $x_\gamma^{\text{obs}} > 0.75$, the NLO QCD predictions describe the data well, although some differences in shape are observed for $d\sigma/d\bar{E}_T$ and $d\sigma/dE_T^{\text{jet1}}$. Although measurements at high x_γ^{obs} are less sensitive to the structure of the photon, it is interesting to note that the prediction using the CJK photon PDF describes the \bar{E}_T spectrum somewhat better. The shapes for the $\bar{\eta}$ and x_p^{obs} distributions are also better reproduced using the CJK photon PDF.

At low x_γ^{obs} , the difference in shapes between data and NLO QCD for $d\sigma/d\bar{E}_T$ and $d\sigma/dE_T^{\text{jet1}}$ is more marked, as has been seen previously [4]. For the prediction using AFG04, the data and NLO agree in the lowest bin whereas the prediction is significantly lower at higher \bar{E}_T and E_T^{jet1} . In contrast, the prediction from CJK is too high in the first bin, which dominates the cross section, but agrees well at higher \bar{E}_T and E_T^{jet1} . For the $\bar{\eta}$ and x_p^{obs} distributions, the shapes are again better described by NLO QCD using the CJK photon PDF, although the normalization is too high. Sensitivity to the photon PDFs is discussed further in Section 8.4.

8.2 Measurement of $d\sigma/d|\Delta\phi^{jj}|$

The cross-section $d\sigma/d|\Delta\phi^{jj}|$ is presented for x_γ^{obs} above and below 0.75 in Tables 10 and 11 and Fig. 8. For $x_\gamma^{\text{obs}} > 0.75$, the cross-section data fall by about three orders of magnitude in the cross section, more steeply than for $x_\gamma^{\text{obs}} \leq 0.75$. The predictions from NLO QCD and also both HERWIG and PYTHIA MC programs (plotted separately since the implementation of parton showers differs between the two programs) are compared to the data. The MC predictions are area normalized to the data in the measured kinematic region. At high x_γ^{obs} , NLO QCD agrees with the data at highest $|\Delta\phi^{jj}|$, but it has a somewhat steeper fall off. The prediction from the PYTHIA MC program is similar to that for NLO QCD, whereas the prediction from the HERWIG program describes the data well. For low x_γ^{obs} , the distribution for NLO QCD is much too steep and is significantly below the data for all values of $|\Delta\phi^{jj}|$ except the highest bin. The prediction from the PYTHIA program is less steep, but still gives a poor description. The prediction from the HERWIG program is in remarkable agreement with the data.

The results and conclusions shown are qualitatively similar to those already seen in dijet photoproduction in which at least one of the jets was tagged as originating from a charm quark [11]. The results here confirm that the parton-shower model in HERWIG gives a good simulation of high-order processes and suggest that a matching of it to NLO QCD would give a good description of the data in both shape and normalization. Should such a calculation or other high-order prediction become available, the distributions presented here would be ideal tests of their validity as they present inclusive quantities and also have higher precision compared to the previous result [11].

8.3 Optimized cross sections

The cross-sections $d\sigma/dx_p^{\text{obs}}$, optimized to be most sensitive to the uncertainty on the gluon PDF in the proton, are given in Tables 12–19 and shown in Figs. 9 and 10 for x_γ^{obs} above and below 0.75, respectively. The measurements cover a range in x_p^{obs} of about 0.1 to 0.5. At high x_γ^{obs} , the data are very well described by NLO QCD predictions. At low x_γ^{obs} , the description by NLO QCD is poorer, particularly when using the AFG04 photon PDF. Generally the predictions with CJK describe the data better with the exception of the “Low- x_γ^{obs} 3” cross section. Inclusion of these high- x_γ^{obs} data in future fits would constrain the proton PDFs further, in particular that of the gluon. To include the cross sections for low x_γ^{obs} , a systematic treatment of the photon PDFs and their uncertainty is needed.

8.4 Sensitivity to the photon PDFs

As discussed in Section 8.1, the measured cross sections show sensitivity to the choice of photon PDFs. This is to be expected due to the extension further forward in pseudorapidity compared to previous measurements. This was investigated further, with the results presented in Figs. 11–13, where predictions with all five available parameterizations of the photon PDFs are compared to the data. In Table 20 and Fig. 11 the cross-section $d\sigma/dx_\gamma^{\text{obs}}$ is shown. At high x_γ^{obs} , all predictions are similar, as expected since there is little sensitivity to the photon structure in this region. Towards low x_γ^{obs} , the predictions differ by up to 70%. The prediction from CJK deviates most from the other predictions and also from the data. The other predictions, although also exhibiting differences between each other of up to 25%, give a qualitatively similar description of the data.

In Figs. 12 and 13, the cross-sections $d\sigma/d\bar{E}_T$, $d\sigma/dx_p^{\text{obs}}$ and $d\sigma/d\bar{\eta}$ are presented for $x_\gamma^{\text{obs}} \leq 0.75$, as shown previously in Figs. 4, 7 and 6, respectively, but here with additional predictions using different photon PDFs. For $d\sigma/d\bar{E}_T$, the prediction using CJK is much higher than the data in the first bin, but then agrees with the data for all subsequent bins. All photon PDFs have a similar shape, and none can reproduce the shape of the measured distribution. Apart from CJK, all PDFs are too low in the region $22.5 < \bar{E}_T < 37.5$ GeV. For the cross-section $d\sigma/dx_p^{\text{obs}}$, no prediction gives a satisfactory description of the data. The prediction from CJK is generally above the data by 20-30%, but describes the shape of the cross section reasonably well. All other predictions give a poor description of the shape, with cross sections which fall too rapidly to high x_p^{obs} . For $d\sigma/d\bar{\eta}$, the prediction from CJK again gives the best description of the shape of the data, although it is too high in normalization.

In summary, the data show a large sensitivity to the parameterization of the photon PDFs. The gluon PDF from CJK, in particular, differs from the others and this may give a hint of how to improve the photon PDFs. The data presented here should significantly improve the measurement of the gluon PDF of the photon, which is currently insufficiently constrained by the F_2^γ data.

9 Conclusions

Dijet cross sections in photoproduction have been measured at high E_T^{jet} and probe a wide range of x_γ^{obs} and x_p^{obs} . The kinematic region is $Q^2 < 1 \text{ GeV}^2$, $142 < W_{\gamma p} < 293 \text{ GeV}$, $E_T^{\text{jet1}} > 20 \text{ GeV}$, $E_T^{\text{jet2}} > 15 \text{ GeV}$ and $-1 < \eta^{\text{jet1,2}} < 3$, with at least one jet lying in the range between -1 and 2.5 . In general, the data enriched in direct-photon events, at high x_γ^{obs} , are well described by NLO QCD predictions. For the data enriched in resolved-photon events, at low x_γ^{obs} , the data are less well described by NLO QCD predictions.

Predictions using different parameterizations of the photon parton density functions give a large spread in the region measured, with no parton density function giving an adequate description of the data. Therefore the data have the potential to improve the constraints on the parton densities in the proton and photon and should be used in future fits. The cross section in the difference of azimuthal angle of the two jets is intrinsically sensitive to high-order QCD processes and the data are poorly described by NLO QCD, particularly at low x_γ^{obs} . Therefore the data should be compared with new calculations of higher orders, or simulations thereof.

10 Acknowledgments

The strong support and encouragement of the DESY Directorate have been invaluable, and we are much indebted to the HERA machine group for their inventiveness and diligent efforts. The design, construction and installation of the ZEUS detector have been made possible by the ingenuity and dedicated efforts of many people from inside DESY and from the home institutes who are not listed as authors. Their contributions are acknowledged with great appreciation. We would also like to thank S. Frixione for help in using his calculation.

References

- [1] ZEUS Coll., M. Derrick et al., Phys. Lett. **B 322**, 287 (1994).
- [2] ZEUS Coll., J. Breitweg et al., Eur. Phys. J. **C 1**, 109 (1998).
- [3] ZEUS Coll., S. Chekanov et al., Phys. Lett. **B 531**, 9 (2002).
- [4] ZEUS Coll., S. Chekanov et al., Eur. Phys. J. **C 23**, 615 (2002).
- [5] ZEUS Coll., M. Derrick et al., Phys. Lett. **B 342**, 417 (1995);
ZEUS Coll., M. Derrick et al., Phys. Lett. **B 348**, 665 (1995);
ZEUS Coll., M. Derrick et al., Phys. Lett. **B 384**, 401 (1995);
ZEUS Coll., J. Breitweg et al., Phys. Lett. **B 443**, 394 (1998);
ZEUS Coll., J. Breitweg et al., Eur. Phys. J. **C 4**, 591 (1998);
ZEUS Coll., J. Breitweg et al., Eur. Phys. J. **C 11**, 35 (1999);
ZEUS Coll., S. Chekanov et al., Phys. Lett. **B 560**, 7 (2003).
- [6] H1 Coll., I. Abt et al., Phys. Lett. **B 314**, 436 (1993);
H1 Coll., S. Aid et al., Z. Phys. **C 70**, 17 (1996);
H1 Coll., C. Adloff et al., Eur. Phys. J. **C 1**, 97 (1998);
H1 Coll., C. Adloff et al., Phys. Lett. **B 483**, 36 (2000);
H1 Coll., C. Adloff et al., Eur. Phys. J. **C 25**, 13 (2002);
H1 Coll., C. Adloff et al., Eur. Phys. J. **C 29**, 497 (2003);
H1 Coll., A. Aktas et al., Phys. Lett. **B 639**, 21 (2006).
- [7] F. Cornet, P. Jankowski and M. Krawczyk, Phys. Rev. **D 70**, 093004 (2004).
- [8] P. Aurenche, M. Fontannaz and J.Ph. Guillet, Eur. Phys. J. **C 34**, 395 (2005).
- [9] W. Slominski, H. Abramowicz and A. Levy, Eur. Phys. J. **C 45**, 633 (2006).
- [10] ZEUS Coll., S. Chekanov et al., Eur. Phys. J. **C 42**, 1 (2005).
- [11] ZEUS Coll., S. Chekanov et al., Nucl. Phys. **B 729**, 492 (2005).
- [12] ZEUS Coll., S. Chekanov et al., Phys. Lett. **B 511**, 19 (2001).
- [13] S. Catani et al., Nucl. Phys. **B 406**, 187 (1993).
- [14] S.D. Ellis and D.E. Soper, Phys. Rev. **D 48**, 3160 (1993).
- [15] C. Targett-Adams, Ph.D. Thesis, University College London, 2006 (unpublished).
- [16] ZEUS Coll., S. Chekanov et al., Phys. Rev. **D 67**, 012007 (2003).
- [17] ZEUS Coll., M. Derrick et al., Phys. Lett. **B 297**, 404 (1992).
- [18] ZEUS Coll., U. Holm (ed.), *The ZEUS Detector*. Status Report (unpublished), DESY (1993), available on <http://www-zeus.desy.de/bluebook/bluebook.html>.

- [19] N. Harnew et al., Nucl. Inst. Meth. **A 279**, 290 (1989);
B. Foster et al., Nucl. Phys. Proc. Suppl. **B 32**, 181 (1993);
B. Foster et al., Nucl. Inst. Meth. **A 338**, 254 (1994).
- [20] M. Derrick et al., Nucl. Inst. Meth. **A 309**, 77 (1991);
A. Andresen et al., Nucl. Inst. Meth. **A 309**, 101 (1991);
A. Caldwell et al., Nucl. Inst. Meth. **A 321**, 356 (1992);
A. Bernstein et al., Nucl. Inst. Meth. **A 336**, 23 (1993).
- [21] J. Andruszków et al., Preprint DESY-92-066, DESY, 1992;
ZEUS Coll., M. Derrick et al., Z. Phys. **C 63**, 391 (1994);
J. Andruszków et al., Acta Phys. Pol. **B 32**, 2025 (2001).
- [22] G. Corcella et al., JHEP **0101**, 010 (2001);
G. Marchesini et al., Comp. Phys. Comm. **67**, 465 (1992).
- [23] T. Sjöstrand et al., Comp. Phys. Comm. **135**, 238 (2001);
T. Sjöstrand, Comp. Phys. Comm. **82**, 74 (1994).
- [24] B.R. Webber, Nucl. Phys. **B 238**, 492 (1984).
- [25] B. Andersson et al., Phys. Rep. **97**, 31 (1983).
- [26] R. Brun et al., GEANT3, Technical Report CERN-DD/EE/84-1, CERN, 1987.
- [27] H.L. Lai et al., Phys. Rev. **D 55**, 1280 (1997).
- [28] M. Glück, E. Reya and A. Vogt, Phys. Rev. **D 45**, 3986 (1992);
M. Glück, E. Reya and A. Vogt, Phys. Rev. **D 46**, 1973 (1992).
- [29] J.M. Butterworth, J.R. Forshaw and M.H. Seymour, Z. Phys. **C 72**, 636 (1996).
- [30] T. Sjöstrand and M. van Zijl, Phys. Rev. **D 36**, 2019 (1987).
- [31] S. Frixione, Z. Kunszt and A. Signer, Nucl. Phys. **B 467**, 399 (1996);
S. Frixione, Nucl. Phys. **B 507**, 295 (1997).
- [32] S. Frixione and G. Ridolfi, Nucl. Phys. **B 507**, 315 (1997).
- [33] R.K. Ellis, D.A. Ross and A.E. Terrano, Nucl. Phys. **B 178**, 421 (1981).
- [34] P. Aurenche, J.P. Guillet and M. Fontannaz, Z. Phys. **C 64**, 621 (1994).
- [35] S. Bethke, Prog. Part. Nucl. Phys. **58**, 351 (2007).
- [36] W.H. Smith, K. Tokushuku and L.W. Wiggers, *Proc. Computing in High-Energy Physics (CHEP), Annecy, France, Sept. 1992*, C. Verkerk and W. Wojcik (eds.), p. 222. CERN, Geneva, Switzerland (1992). Also in preprint DESY 92-150B.
- [37] F. Jacquet and A. Blondel, *Proceedings of the Study for an ep Facility for Europe*, U. Amaldi (ed.), p. 391. Hamburg, Germany (1979). Also in preprint DESY 79/48.

- [38] M. Wing (on behalf of the ZEUS Coll.), *Proc. of the 10th International Conference on Calorimetry in High Energy Physics*, R. Zhu (ed.), p. 767. Pasadena, USA (2002). Also in preprint hep-ex/0206036.
- [39] H. Perrey, Diploma Thesis, Universität Hamburg, 2007 (unpublished).
- [40] K. Hagiwara et al., *Phys. Rev. D* **51**, 3197 (1995).

Label	x_γ^{obs} cut	$\eta^{\text{jet1,2}}$ cuts	$E_T^{\text{jet1,2}}$ cuts
“High- x_γ^{obs} 1”	$x_\gamma^{\text{obs}} > 0.75$	$0 < \eta^{\text{jet1}} < 1, 2 < \eta^{\text{jet2}} < 3$	$E_T^{\text{jet1,2}} > 25, 15 \text{ GeV}$
“High- x_γ^{obs} 2”	$x_\gamma^{\text{obs}} > 0.75$	$0 < \eta^{\text{jet1}} < 1, 2 < \eta^{\text{jet2}} < 3$	$E_T^{\text{jet1,2}} > 20, 15 \text{ GeV}$
“High- x_γ^{obs} 3”	$x_\gamma^{\text{obs}} > 0.75$	$1 < \eta^{\text{jet1,2}} < 2$	$E_T^{\text{jet1,2}} > 30, 15 \text{ GeV}$
“High- x_γ^{obs} 4”	$x_\gamma^{\text{obs}} > 0.75$	$-1 < \eta^{\text{jet1}} < 0, 0 < \eta^{\text{jet2}} < 1$	$E_T^{\text{jet1,2}} > 20, 15 \text{ GeV}$
“Low- x_γ^{obs} 1”	$x_\gamma^{\text{obs}} < 0.75$	$2 < \eta^{\text{jet1}} < 2.5, 2 < \eta^{\text{jet2}} < 3$	$E_T^{\text{jet1,2}} > 20, 15 \text{ GeV}$
“Low- x_γ^{obs} 2”	$x_\gamma^{\text{obs}} < 0.75$	$1 < \eta^{\text{jet1,2}} < 2$	$E_T^{\text{jet1,2}} > 25, 15 \text{ GeV}$
“Low- x_γ^{obs} 3”	$x_\gamma^{\text{obs}} < 0.75$	$1 < \eta^{\text{jet1}} < 2, 2 < \eta^{\text{jet2}} < 3$	$E_T^{\text{jet1,2}} > 20, 15 \text{ GeV}$
“Low- x_γ^{obs} 4”	$x_\gamma^{\text{obs}} < 0.75$	$1 < \eta^{\text{jet1}} < 2, 2 < \eta^{\text{jet2}} < 3$	$E_T^{\text{jet1,2}} > 25, 15 \text{ GeV}$

Table 1: Kinematic regions of the “optimized” cross sections.

\bar{E}_T bin (GeV)	$d\sigma/d\bar{E}_T$	δ_{stat}	δ_{MC}	δ_{syst}	δ_{ES}	(pb/GeV)	C_{had}
17.5, 22.5	25.73	± 0.36	+0.66 -0.00	+0.41 -0.43	+1.03 -1.20		0.955 ± 0.017
22.5, 27.5	14.66	± 0.28	+0.00 -0.28	+0.42 -0.26	+0.60 -0.65		0.931 ± 0.008
27.5, 32.5	5.57	± 0.18	+0.09 -0.00	+0.14 -0.24	+0.30 -0.19		0.937 ± 0.029
32.5, 37.5	2.37	± 0.12	+0.00 -0.03	+0.15 -0.04	+0.11 -0.11		0.927 ± 0.012
37.5, 42.5	0.96	± 0.07	+0.02 -0.00	+0.06 -0.03	+0.07 -0.03		0.907 ± 0.034
42.5, 55.5	0.300	± 0.024	+0.000 -0.004	+0.004 -0.018	+0.016 -0.020		0.932 ± 0.044
55.5, 70.5	0.046	± 0.009	+0.006 -0.000	+0.001 -0.003	+0.003 -0.003		0.926 ± 0.029
70.5, 90.5	0.009	± 0.004	+0.001 -0.000	+0.001 -0.002	+0.000 -0.002		0.917 ± 0.085

Table 2: Measured cross-section $d\sigma/d\bar{E}_T$ for $x_\gamma^{\text{obs}} > 0.75$. The statistical, δ_{stat} , MC model, δ_{MC} , uncorrelated systematic, δ_{syst} , and jet energy scale, δ_{ES} , uncertainties are shown separately. The hadronization correction factor, C_{had} , applied to the NLO QCD prediction is shown in the last column, where its uncertainty is half the spread between the values obtained using the HERWIG and PYTHIA models.

\bar{E}_T bin (GeV)	$d\sigma/d\bar{E}_T$	δ_{stat}	δ_{MC}	δ_{syst}	δ_{ES}	(pb/GeV)	C_{had}
17.5, 22.5	27.10	± 0.36	+0.49 -0.00	+0.18 -1.31	+1.45 -1.42		1.082 ± 0.045
22.5, 27.5	11.97	± 0.24	+0.07 -0.00	+0.21 -0.66	+0.56 -0.74		1.047 ± 0.009
27.5, 32.5	3.69	± 0.14	+0.17 -0.00	+0.10 -0.23	+0.27 -0.18		1.057 ± 0.016
32.5, 37.5	1.24	± 0.08	+0.03 -0.00	+0.06 -0.12	+0.07 -0.09		1.004 ± 0.024
37.5, 42.5	0.46	± 0.05	+0.03 -0.00	+0.01 -0.05	+0.04 -0.03		1.069 ± 0.043
42.5, 55.5	0.090	± 0.013	+0.005 -0.000	+0.009 -0.010	+0.008 -0.007		1.019 ± 0.015
55.5, 70.5	0.011	± 0.005	+0.004 -0.000	+0.006 -0.002	+0.001 -0.001		0.974 ± 0.064

Table 3: Measured cross-section $d\sigma/d\bar{E}_T$ for $x_\gamma^{\text{obs}} \leq 0.75$. For further details, see the caption to Table 2.

E_T^{jet1} bin (GeV)	$d\sigma/dE_T^{\text{jet1}}$	δ_{stat}	δ_{MC}	δ_{syst}	δ_{ES}	(pb/GeV)	C_{had}
20, 26	27.24	± 0.33	+0.18 -0.00	+0.56 -0.54	+1.05 -1.22		0.957 ± 0.021
26, 32	9.21	± 0.20	+0.17 -0.00	+0.21 -0.15	+0.49 -0.37		0.920 ± 0.011
32, 38	3.34	± 0.12	+0.00 -0.05	+0.16 -0.12	+0.14 -0.17		0.916 ± 0.024
38, 44	1.25	± 0.07	+0.03 -0.00	+0.15 -0.03	+0.07 -0.06		0.943 ± 0.005
44, 55	0.37	± 0.03	+0.00 -0.00	+0.01 -0.03	+0.02 -0.03		0.921 ± 0.035
55, 70	0.056	± 0.009	+0.008 -0.000	+0.004 -0.003	+0.007 -0.002		0.889 ± 0.051
70, 90	0.010	± 0.004	+0.004 -0.000	+0.004 -0.001	+0.002 -0.000		0.85 ± 0.11

Table 4: Measured cross-section $d\sigma/dE_T^{\text{jet1}}$ for $x_\gamma^{\text{obs}} > 0.75$. For further details, see the caption to Table 2.

E_T^{jet1} bin (GeV)	$d\sigma/dE_T^{\text{jet1}}$	δ_{stat}	δ_{MC}	δ_{syst}	δ_{ES}	(pb/GeV)	C_{had}
20, 26	25.59	± 0.31	+0.43 -0.00	+0.21 -1.33	+1.32 -1.34		1.081 ± 0.043
26, 32	8.11	± 0.18	+0.21 -0.00	+0.10 -0.41	+0.49 -0.47		1.041 ± 0.015
32, 38	2.39	± 0.10	+0.06 -0.00	+0.10 -0.17	+0.14 -0.15		1.017 ± 0.025
38, 44	0.72	± 0.05	+0.00 -0.01	+0.02 -0.05	+0.04 -0.05		0.997 ± 0.006
44, 55	0.18	± 0.02	+0.02 -0.00	+0.01 -0.02	+0.02 -0.01		0.963 ± 0.027
55, 70	0.018	± 0.006	+0.001 -0.000	+0.004 -0.003	+0.001 -0.002		0.927 ± 0.033

Table 5: Measured cross-section $d\sigma/dE_T^{\text{jet1}}$ for $x_\gamma^{\text{obs}} \leq 0.75$. For further details, see the caption to Table 2.

$\bar{\eta}$ bin	$d\sigma/d\bar{\eta}$	δ_{stat}	δ_{MC}	δ_{syst}	δ_{ES}	(pb)	C_{had}
-0.50, 0.00	4.8	± 1.2	+0.2 -0.0	+0.7 -1.4	+0.7 -1.6		0.551 ± 0.037
0.00, 0.50	90.1	± 2.3	+5.1 -0.0	+4.0 -1.2	+6.8 -5.3		0.892 ± 0.018
0.50, 1.00	177.8	± 2.9	+2.5 -0.0	+2.6 -3.6	+7.1 -8.9		0.940 ± 0.001
1.00, 1.50	167.6	± 2.6	+0.0 -1.2	+6.5 -3.1	+6.6 -6.5		0.952 ± 0.014
1.50, 2.00	59.0	± 1.5	+0.6 -0.0	+0.7 -0.6	+1.4 -1.5		1.079 ± 0.035
2.00, 2.50	2.8	± 0.5	+0.0 -0.2	+0.1 -0.3	+0.0 -0.0		1.062 ± 0.064

Table 6: Measured cross-section $d\sigma/d\bar{\eta}$ for $x_\gamma^{\text{obs}} > 0.75$. For further details, see the caption to Table 2.

$\bar{\eta}$ bin	$d\sigma/d\bar{\eta}$	δ_{stat}	δ_{MC}	δ_{syst}	δ_{ES}	(pb)	C_{had}
0.00, 0.50	7.2	± 0.8	+0.0 -0.1	+0.7 -0.9	+0.9 -0.8		1.052 ± 0.080
0.50, 1.00	65.9	± 1.9	+0.0 -0.0	+1.5 -5.1	+4.1 -5.1		1.074 ± 0.054
1.00, 1.50	144.0	± 2.6	+3.2 -0.0	+1.7 -7.6	+7.6 -8.1		1.080 ± 0.021
1.50, 2.00	146.8	± 2.4	+1.6 -0.0	+2.2 -7.8	+7.2 -7.2		1.063 ± 0.019
2.00, 2.50	71.3	± 1.7	+5.1 -0.0	+2.2 -2.5	+4.0 -2.9		1.062 ± 0.022
2.50, 2.75	18.4	± 1.5	+0.7 -0.0	+0.3 -2.6	+0.4 -1.5		1.066 ± 0.002

Table 7: Measured cross-section $d\sigma/d\bar{\eta}$ for $x_\gamma^{\text{obs}} \leq 0.75$. For further details, see the caption to Table 2.

x_p^{obs} bin	$d\sigma/dx_p^{\text{obs}}$	δ_{stat}	δ_{MC}	δ_{syst}	δ_{ES}	(pb)	C_{had}
0.00, 0.05	1260	± 26	+57 -0	+21 -23	+69 -72		0.902 ± 0.025
0.05, 0.10	1960	± 30	+7 -0	+35 -48	+81 -82		0.932 ± 0.007
0.10, 0.15	925	± 20	+0 -1	+60 -12	+27 -41		0.996 ± 0.024
0.15, 0.20	468	± 15	+0 -9	+13 -7	+24 -17		0.999 ± 0.015
0.20, 0.25	220	± 11	+0 -4	+12 -5	+6 -9		0.982 ± 0.012
0.25, 0.30	104.9	± 8.4	+0.0 -1.3	+2.9 -10.8	+5.1 -4.1		0.963 ± 0.015
0.30, 0.35	45.0	± 5.6	+1.5 -0.0	+3.4 -1.0	+2.4 -1.2		1.063 ± 0.023
0.35, 0.40	23.2	± 4.1	+0.0 -0.9	+0.5 -0.9	+0.6 -1.6		1.027 ± 0.008
0.40, 0.45	8.7	± 2.4	+0.9 -0.0	+4.0 -0.5	+1.0 -0.1		1.010 ± 0.020
0.45, 0.50	3.2	± 1.4	+0.0 -0.3	+2.5 -1.0	+0.2 -0.2		1.006 ± 0.016
0.50, 1.00	0.40	± 0.17	+0.08 -0.00	+0.08 -0.21	+0.06 -0.01		0.987 ± 0.018

Table 8: Measured cross-section $d\sigma/dx_p^{\text{obs}}$ for $x_\gamma^{\text{obs}} > 0.75$. For further details, see the caption to Table 2.

x_p^{obs} bin	$d\sigma/dx_p^{\text{obs}}$	δ_{stat}	δ_{MC}	δ_{syst}	δ_{ES}	(pb)	C_{had}
0.00, 0.05	236	± 12	$\begin{smallmatrix} +2 \\ -0 \end{smallmatrix}$	$\begin{smallmatrix} +17 \\ -24 \end{smallmatrix}$	$\begin{smallmatrix} +18 \\ -19 \end{smallmatrix}$		1.103 ± 0.092
0.05, 0.10	1131	± 24	$\begin{smallmatrix} +0 \\ -0 \end{smallmatrix}$	$\begin{smallmatrix} +19 \\ -76 \end{smallmatrix}$	$\begin{smallmatrix} +55 \\ -70 \end{smallmatrix}$		1.063 ± 0.046
0.10, 0.15	1120	± 22	$\begin{smallmatrix} +19 \\ -0 \end{smallmatrix}$	$\begin{smallmatrix} +37 \\ -63 \end{smallmatrix}$	$\begin{smallmatrix} +56 \\ -61 \end{smallmatrix}$		1.086 ± 0.022
0.15, 0.20	829	± 19	$\begin{smallmatrix} +12 \\ -0 \end{smallmatrix}$	$\begin{smallmatrix} +7 \\ -37 \end{smallmatrix}$	$\begin{smallmatrix} +46 \\ -37 \end{smallmatrix}$		1.074 ± 0.001
0.20, 0.25	581	± 17	$\begin{smallmatrix} +14 \\ -0 \end{smallmatrix}$	$\begin{smallmatrix} +5 \\ -49 \end{smallmatrix}$	$\begin{smallmatrix} +31 \\ -30 \end{smallmatrix}$		1.053 ± 0.001
0.25, 0.30	302	± 12	$\begin{smallmatrix} +31 \\ -0 \end{smallmatrix}$	$\begin{smallmatrix} +25 \\ -10 \end{smallmatrix}$	$\begin{smallmatrix} +17 \\ -13 \end{smallmatrix}$		1.052 ± 0.052
0.30, 0.35	146.8	± 9.4	$\begin{smallmatrix} +8.3 \\ -0.0 \end{smallmatrix}$	$\begin{smallmatrix} +4.2 \\ -6.2 \end{smallmatrix}$	$\begin{smallmatrix} +7.0 \\ -9.7 \end{smallmatrix}$		1.052 ± 0.014
0.35, 0.40	65.5	± 6.6	$\begin{smallmatrix} +0.0 \\ -0.3 \end{smallmatrix}$	$\begin{smallmatrix} +0.6 \\ -15.0 \end{smallmatrix}$	$\begin{smallmatrix} +3.9 \\ -4.2 \end{smallmatrix}$		1.041 ± 0.008
0.40, 0.45	24.6	± 4.2	$\begin{smallmatrix} +1.1 \\ -0.0 \end{smallmatrix}$	$\begin{smallmatrix} +4.8 \\ -2.2 \end{smallmatrix}$	$\begin{smallmatrix} +0.4 \\ -3.0 \end{smallmatrix}$		1.036 ± 0.004
0.45, 0.50	9.6	± 2.7	$\begin{smallmatrix} +0.0 \\ -0.7 \end{smallmatrix}$	$\begin{smallmatrix} +0.7 \\ -2.3 \end{smallmatrix}$	$\begin{smallmatrix} +1.7 \\ -0.2 \end{smallmatrix}$		1.020 ± 0.005
0.50, 1.00	0.86	± 0.27	$\begin{smallmatrix} +0.09 \\ -0.00 \end{smallmatrix}$	$\begin{smallmatrix} +0.32 \\ -0.09 \end{smallmatrix}$	$\begin{smallmatrix} +0.07 \\ -0.10 \end{smallmatrix}$		1.012 ± 0.034

Table 9: Measured cross-section $d\sigma/dx_p^{\text{obs}}$ for $x_\gamma^{\text{obs}} \leq 0.75$. For further details, see the caption to Table 2.

$ \Delta\phi^{\text{jj}} $ bin	$d\sigma/d \Delta\phi^{\text{jj}} $	δ_{stat}	δ_{MC}	δ_{syst}	δ_{ES}	(pb/rad)	C_{had}
1.83, 2.09	1.7	± 0.5	$\begin{smallmatrix} +0.1 \\ -0.0 \end{smallmatrix}$	$\begin{smallmatrix} +0.2 \\ -0.5 \end{smallmatrix}$	$\begin{smallmatrix} +0.1 \\ -0.2 \end{smallmatrix}$		0.65 ± 0.11
2.09, 2.36	7.8	± 1.0	$\begin{smallmatrix} +0.0 \\ -0.0 \end{smallmatrix}$	$\begin{smallmatrix} +1.2 \\ -0.6 \end{smallmatrix}$	$\begin{smallmatrix} +0.6 \\ -0.6 \end{smallmatrix}$		0.729 ± 0.059
2.36, 2.62	36.1	± 2.2	$\begin{smallmatrix} +0.2 \\ -0.0 \end{smallmatrix}$	$\begin{smallmatrix} +1.6 \\ -1.7 \end{smallmatrix}$	$\begin{smallmatrix} +2.1 \\ -1.8 \end{smallmatrix}$		0.826 ± 0.013
2.62, 2.88	132.9	± 3.9	$\begin{smallmatrix} +5.8 \\ -0.0 \end{smallmatrix}$	$\begin{smallmatrix} +5.9 \\ -2.7 \end{smallmatrix}$	$\begin{smallmatrix} +6.6 \\ -8.3 \end{smallmatrix}$		0.868 ± 0.008
2.88, 3.14	779.1	± 8.1	$\begin{smallmatrix} +4.0 \\ -0.0 \end{smallmatrix}$	$\begin{smallmatrix} +15.0 \\ -13.3 \end{smallmatrix}$	$\begin{smallmatrix} +31.8 \\ -33.6 \end{smallmatrix}$		0.984 ± 0.015

Table 10: Measured cross-section $d\sigma/d|\Delta\phi^{\text{jj}}|$ for $x_\gamma^{\text{obs}} > 0.75$. For further details, see the caption to Table 2.

$ \Delta\phi^{\text{jj}} $ bin	$d\sigma/d \Delta\phi^{\text{jj}} $	δ_{stat}	δ_{MC}	δ_{syst}	δ_{ES}	(pb/rad)	C_{had}
0.00, 1.57	0.26	± 0.07	$\begin{smallmatrix} +0.05 \\ -0.00 \end{smallmatrix}$	$\begin{smallmatrix} +0.02 \\ -0.02 \end{smallmatrix}$	$\begin{smallmatrix} +0.04 \\ -0.02 \end{smallmatrix}$		0.84 ± 0.15
1.57, 1.83	2.9	± 0.6	$\begin{smallmatrix} +0.3 \\ -0.0 \end{smallmatrix}$	$\begin{smallmatrix} +0.6 \\ -0.1 \end{smallmatrix}$	$\begin{smallmatrix} +0.1 \\ -0.3 \end{smallmatrix}$		0.869 ± 0.083
1.83, 2.09	6.6	± 0.8	$\begin{smallmatrix} +0.2 \\ -0.0 \end{smallmatrix}$	$\begin{smallmatrix} +0.4 \\ -0.2 \end{smallmatrix}$	$\begin{smallmatrix} +0.3 \\ -0.6 \end{smallmatrix}$		0.910 ± 0.031
2.09, 2.36	28.2	± 1.7	$\begin{smallmatrix} +0.0 \\ -0.5 \end{smallmatrix}$	$\begin{smallmatrix} +0.6 \\ -2.3 \end{smallmatrix}$	$\begin{smallmatrix} +2.4 \\ -1.3 \end{smallmatrix}$		0.959 ± 0.004
2.36, 2.62	78.4	± 2.8	$\begin{smallmatrix} +1.2 \\ -0.0 \end{smallmatrix}$	$\begin{smallmatrix} +3.5 \\ -1.0 \end{smallmatrix}$	$\begin{smallmatrix} +4.3 \\ -5.3 \end{smallmatrix}$		0.988 ± 0.006
2.62, 2.88	203.2	± 4.5	$\begin{smallmatrix} +0.0 \\ -1.1 \end{smallmatrix}$	$\begin{smallmatrix} +0.6 \\ -8.6 \end{smallmatrix}$	$\begin{smallmatrix} +10.4 \\ -13.4 \end{smallmatrix}$		1.006 ± 0.015
2.88, 3.14	528.6	± 6.7	$\begin{smallmatrix} +16.5 \\ -0.0 \end{smallmatrix}$	$\begin{smallmatrix} +6.0 \\ -36.5 \end{smallmatrix}$	$\begin{smallmatrix} +28.1 \\ -26.4 \end{smallmatrix}$		1.069 ± 0.020

Table 11: Measured cross-section $d\sigma/d|\Delta\phi^{\text{jj}}|$ for $x_\gamma^{\text{obs}} \leq 0.75$. For further details, see the caption to Table 2.

x_p^{obs} bin	$d\sigma/dx_p^{\text{obs}}$	δ_{stat}	δ_{MC}	δ_{syst}	δ_{ES}	(pb)	C_{had}
0.1, 0.2	80.9	± 4.2	+0.0 -3.4	+3.8 -6.1	+3.8 -3.4		0.957 ± 0.010
0.2, 0.3	51.6	± 3.5	+0.0 -1.0	+3.1 -2.0	+2.4 -2.1		0.974 ± 0.059
0.3, 0.4	12.6	± 2.1	+0.0 -0.0	+1.0 -0.9	+0.6 -0.9		0.962 ± 0.010
0.4, 0.5	2.1	± 1.0	+1.0 -0.0	+1.0 -0.3	+0.2 -0.1		0.953 ± 0.024

Table 12: Measured cross-section $d\sigma/dx_p^{\text{obs}}$ for $x_\gamma^{\text{obs}} > 0.75$ (“High- x_γ^{obs} 1”). For further details, see the caption to Table 2.

x_p^{obs} bin	$d\sigma/dx_p^{\text{obs}}$	δ_{stat}	δ_{MC}	δ_{syst}	δ_{ES}	(pb)	C_{had}
0.0, 0.1	10.1	± 1.6	+0.1 -0.0	+0.6 -0.5	+0.7 -0.2		0.961 ± 0.037
0.1, 0.2	238.9	± 7.1	+0.0 -5.2	+15.0 -6.8	+9.7 -10.8		1.006 ± 0.021
0.2, 0.3	77.0	± 4.5	+0.0 -2.4	+6.7 -1.9	+3.6 -2.7		1.005 ± 0.026
0.3, 0.4	12.6	± 2.1	+0.0 -0.0	+0.9 -0.9	+0.6 -0.9		0.964 ± 0.009
0.4, 0.5	2.1	± 1.0	+1.0 -0.0	+1.0 -0.3	+0.2 -0.1		0.953 ± 0.024

Table 13: Measured cross-section $d\sigma/dx_p^{\text{obs}}$ for $x_\gamma^{\text{obs}} > 0.75$ (“High- x_γ^{obs} 2”). For further details, see the caption to Table 2.

x_p^{obs} bin	$d\sigma/dx_p^{\text{obs}}$	δ_{stat}	δ_{MC}	δ_{syst}	δ_{ES}	(pb)	C_{had}
0.0, 0.1	2.1	± 0.8	+0.4 -0.0	+1.4 -0.1	+0.1 -0.1		0.914 ± 0.014
0.1, 0.2	55.9	± 3.5	+0.1 -0.0	+1.2 -2.7	+2.3 -1.4		0.974 ± 0.006
0.2, 0.3	20.5	± 2.1	+0.9 -0.0	+0.3 -3.0	+0.7 -0.8		0.988 ± 0.011
0.3, 0.4	2.4	± 0.7	+0.0 -0.0	+0.1 -0.4	+0.1 -0.1		1.007 ± 0.046

Table 14: Measured cross-section $d\sigma/dx_p^{\text{obs}}$ for $x_\gamma^{\text{obs}} > 0.75$ (“High- x_γ^{obs} 3”). For further details, see the caption to Table 2.

x_p^{obs} bin	$d\sigma/dx_p^{\text{obs}}$	δ_{stat}	δ_{MC}	δ_{syst}	δ_{ES}	(pb)	C_{had}
0.0, 0.1	198.0	± 8.8	+10.9 -0.0	+2.9 -2.3	+18.7 -16.0		0.832 ± 0.017

Table 15: Measured cross-section $d\sigma/dx_p^{\text{obs}}$ for $x_\gamma^{\text{obs}} > 0.75$ (“High- x_γ^{obs} 4”). For further details, see the caption to Table 2.

x_p^{obs} bin	$d\sigma/dx_p^{\text{obs}}$	δ_{stat}	δ_{MC}	δ_{syst}	δ_{ES}	(pb)	C_{had}
0.1, 0.2	15.0	± 2.0	$+0.8$ -0.0	$+2.2$ -0.5	$+0.5$ -0.3		1.004 ± 0.099
0.2, 0.3	89.4	± 4.6	$+13.4$ -0.0	$+1.5$ -4.1	$+4.3$ -3.9		1.030 ± 0.003
0.3, 0.4	46.7	± 3.8	$+2.3$ -0.0	$+0.4$ -4.3	$+1.8$ -3.3		1.070 ± 0.090
0.4, 0.5	7.0	± 1.5	$+0.4$ -0.0	$+0.2$ -0.6	$+0.1$ -0.9		0.960 ± 0.083
0.5, 1.0	0.48	± 0.20	$+0.00$ -0.04	$+0.04$ -0.09	$+0.03$ -0.05		1.024 ± 0.027

Table 16: Measured cross-section $d\sigma/dx_p^{\text{obs}}$ for $x_\gamma^{\text{obs}} \leq 0.75$ (“Low- x_γ^{obs} 1”). For further details, see the caption to Table 2.

x_p^{obs} bin	$d\sigma/dx_p^{\text{obs}}$	δ_{stat}	δ_{MC}	δ_{syst}	δ_{ES}	(pb)	C_{had}
0.0, 0.1	19.5	± 2.3	$+1.5$ -0.0	$+0.8$ -3.0	$+0.4$ -1.8		0.876 ± 0.076
0.1, 0.2	117.6	± 5.0	$+2.0$ -0.0	$+4.7$ -9.7	$+5.5$ -5.3		1.048 ± 0.014
0.2, 0.3	12.6	± 1.7	$+0.6$ -0.0	$+0.6$ -1.9	$+0.7$ -0.7		1.116 ± 0.085

Table 17: Measured cross-section $d\sigma/dx_p^{\text{obs}}$ for $x_\gamma^{\text{obs}} \leq 0.75$ (“Low- x_γ^{obs} 2”). For further details, see the caption to Table 2.

x_p^{obs} bin	$d\sigma/dx_p^{\text{obs}}$	δ_{stat}	δ_{MC}	δ_{syst}	δ_{ES}	(pb)	C_{had}
0.1, 0.2	278.4	± 7.6	$+4.2$ -0.0	$+4.6$ -12.7	$+13.5$ -12.4		1.087 ± 0.015
0.2, 0.3	235.2	± 7.1	$+10.3$ -0.0	$+2.1$ -9.6	$+12.2$ -10.3		1.077 ± 0.030
0.3, 0.4	47.8	± 3.6	$+0.7$ -0.0	$+0.8$ -3.4	$+2.8$ -2.6		0.999 ± 0.064
0.4, 0.5	8.3	± 1.6	$+0.0$ -0.1	$+1.7$ -0.6	$+0.7$ -0.6		1.037 ± 0.020
0.5, 1.0	0.28	± 0.14	$+0.15$ -0.0	$+0.19$ -0.04	$+0.07$ -0.01		1.003 ± 0.037

Table 18: Measured cross-section $d\sigma/dx_p^{\text{obs}}$ for $x_\gamma^{\text{obs}} \leq 0.75$ (“Low- x_γ^{obs} 3”). For further details, see the caption to Table 2.

x_p^{obs} bin	$d\sigma/dx_p^{\text{obs}}$	δ_{stat}	δ_{MC}	δ_{syst}	δ_{ES}	(pb)	C_{had}
0.1, 0.2	71.3	± 4.1	$+1.8$ -0.0	$+2.6$ -4.6	$+4.2$ -3.4		1.066 ± 0.052
0.2, 0.3	120.4	± 5.0	$+5.6$ -0.0	$+2.6$ -6.3	$+7.3$ -4.6		1.042 ± 0.021
0.3, 0.4	45.0	± 3.4	$+0.3$ -0.0	$+1.9$ -3.3	$+1.8$ -3.2		1.013 ± 0.059
0.4, 0.5	8.3	± 1.6	$+0.0$ -0.1	$+1.7$ -0.6	$+0.7$ -0.6		1.037 ± 0.020
0.5, 1.0	0.28	± 0.14	$+0.15$ -0.00	$+0.19$ -0.04	$+0.07$ -0.01		1.003 ± 0.037

Table 19: Measured cross-section $d\sigma/dx_p^{\text{obs}}$ for $x_\gamma^{\text{obs}} \leq 0.75$ (“Low- x_γ^{obs} 4”). For further details, see the caption to Table 2.

x_γ^{obs} bin	$d\sigma/dx_\gamma^{\text{obs}}$	δ_{stat}	δ_{MC}	δ_{syst}	δ_{ES}	(pb)	C_{had}
0.1, 0.2	169.5	± 6.8	+19.6 -0.0	+2.3 -7.4	+14.7 -12.6		1.081 ± 0.046
0.2, 0.3	271.6	± 8.0	+12.0 -0.0	+1.7 -8.2	+17.1 -14.3		1.042 ± 0.056
0.3, 0.4	325.7	± 8.9	+0.3 -0.0	+2.5 -15.2	+16.2 -16.3		1.065 ± 0.017
0.4, 0.5	346.6	± 9.3	+7.2 -0.0	+7.6 -15.3	+17.2 -19.0		1.058 ± 0.023
0.5, 0.6	385	± 10	+3 -0	+4 -21	+20 -19		1.072 ± 0.016
0.6, 0.7	458	± 11	+3 -0	+17 -30	+20 -24		1.089 ± 0.028
0.7, 0.8	557	± 12	+1 -0	+16 -55	+28 -29		1.087 ± 0.011
0.8, 1.0	1106	± 11	+15 -0	+32 -21	+47 -48		0.940 ± 0.018

Table 20: Measured cross-section $d\sigma/dx_\gamma^{\text{obs}}$. For further details, see the caption to Table 2.

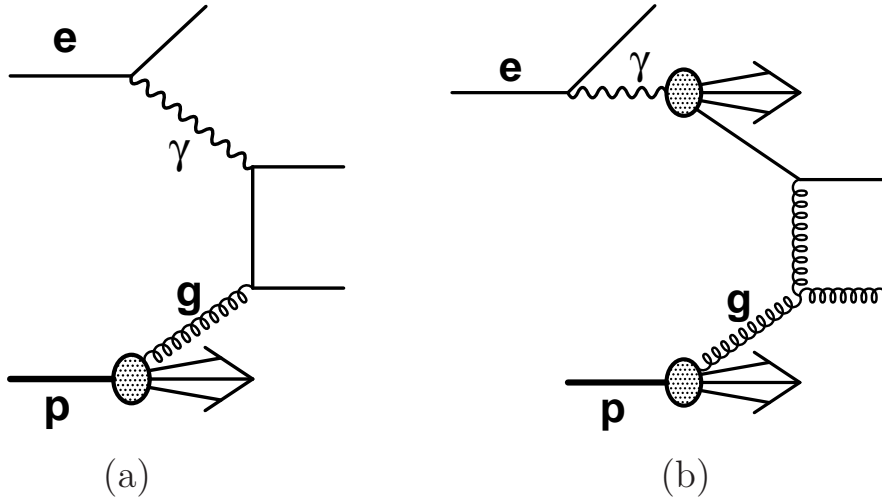


Figure 1: Examples of (a) direct and (b) resolved dijet photoproduction diagrams in positron-proton, ep , collisions in LO QCD. This direct-photon process is the collision of a photon, γ , and gluon, g from the proton. This resolved-photon process is a collision of a parton from the photon and a gluon, g , from the proton.

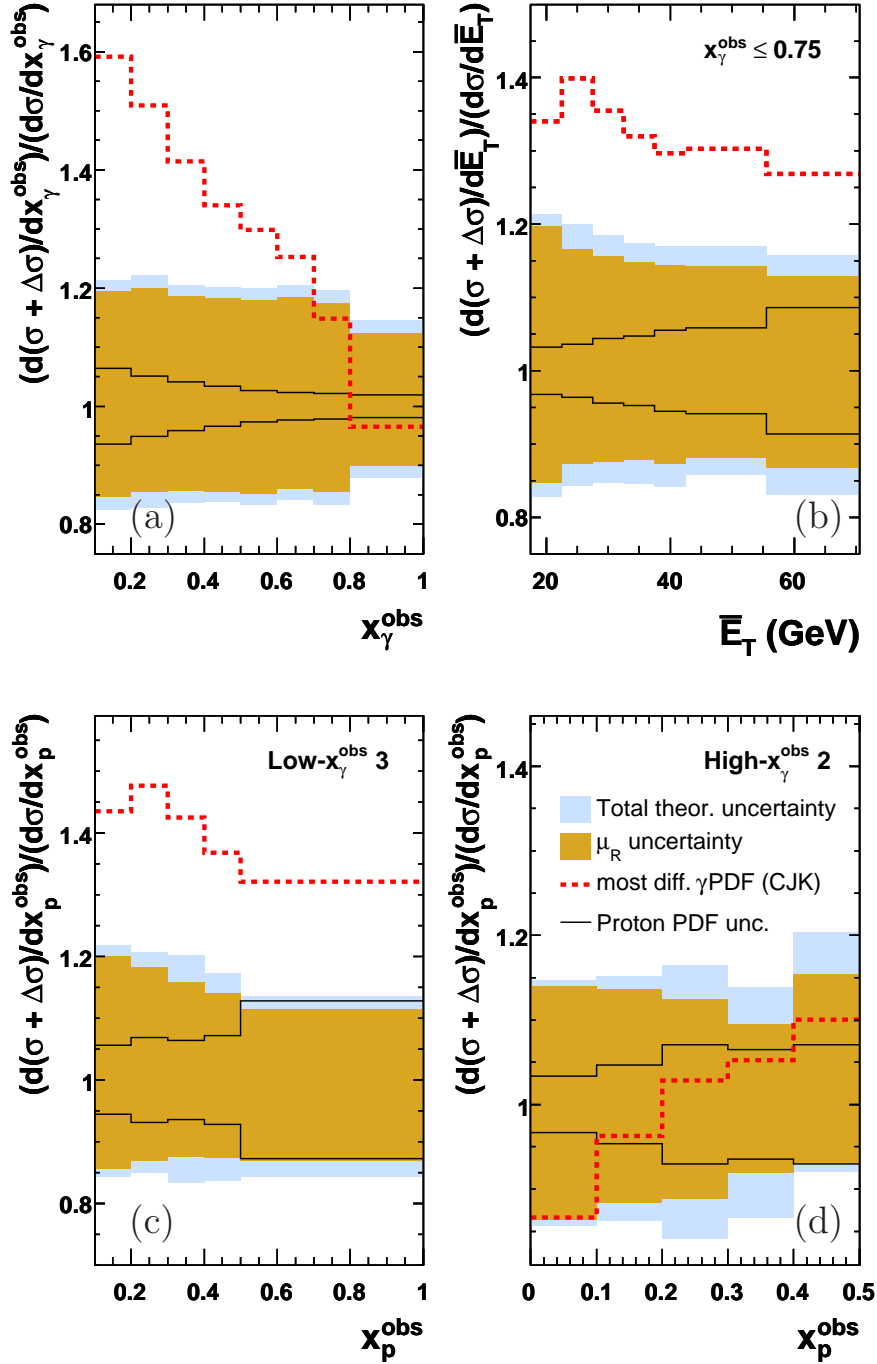


Figure 2: The theoretical uncertainties (see Section 5) for sample distributions: (a) x_γ^{obs} , (b) \bar{E}_T for $x_\gamma^{\text{obs}} \leq 0.75$, (c) “Low- x_γ^{obs} 3” and (d) “High- x_γ^{obs} 2”, which are defined in Table 1. The uncertainties are the total (outer shaded band), that from varying μ_R (inner shaded band), the experimental uncertainties of data propagated in the ZEUS-JETS fit (solid lines) and using the most different photon PDF, CJK (dashed line) instead of AFG04.

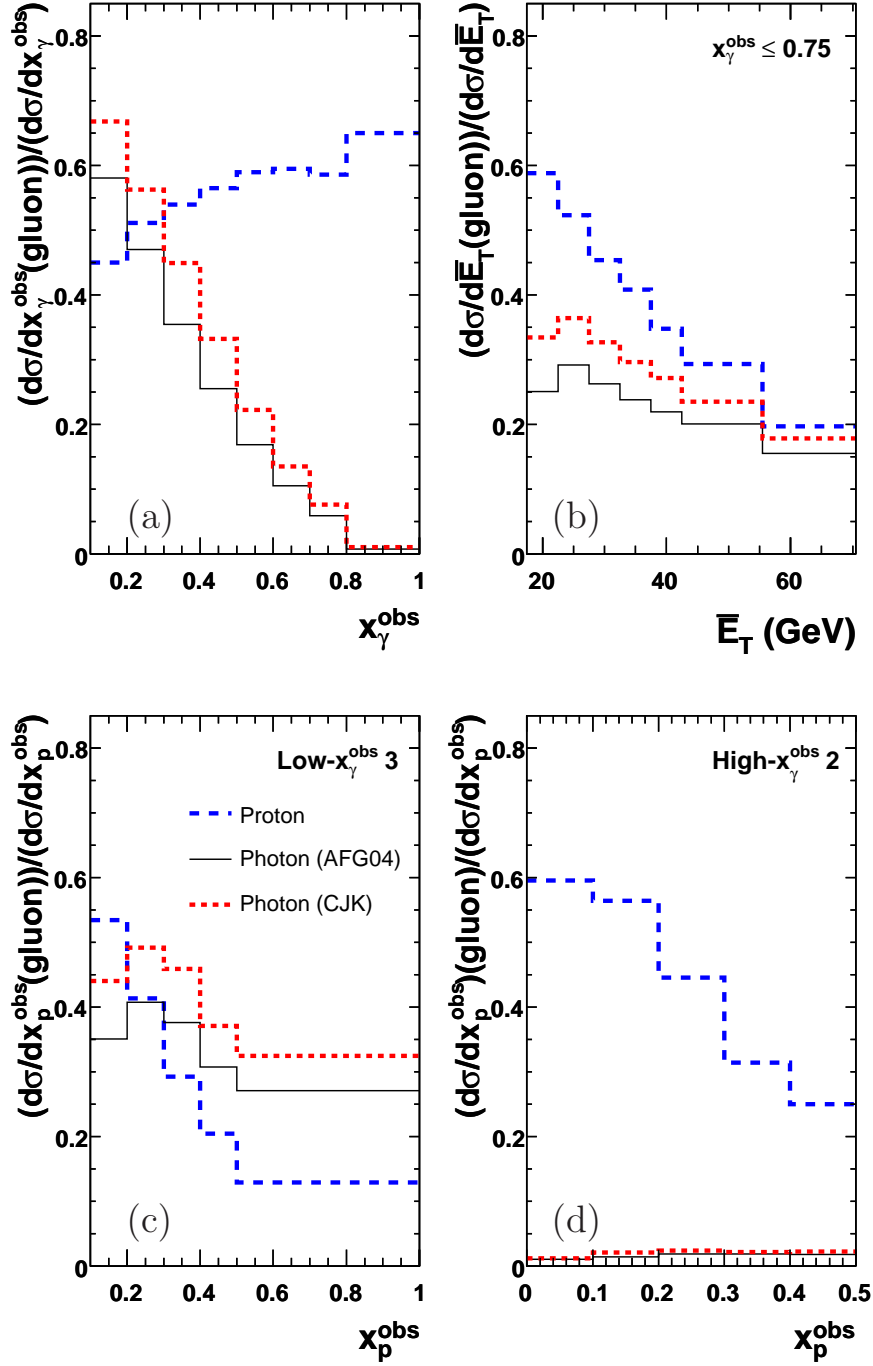


Figure 3: Predictions of the fraction of the cross section initiated by gluons for sample distributions: (a) x_γ^{obs} , (b) \bar{E}_T for $x_\gamma^{\text{obs}} \leq 0.75$, (c) “Low- x_γ^{obs} 3” and (d) “High- x_γ^{obs} 2”, which are defined in Table 1. The gluon fractions are from the proton using the CTEQ5M1 PDF (long-dashed line), and from the photon using the AFG04 (solid line) and CJK PDFs (short-dashed line).

ZEUS

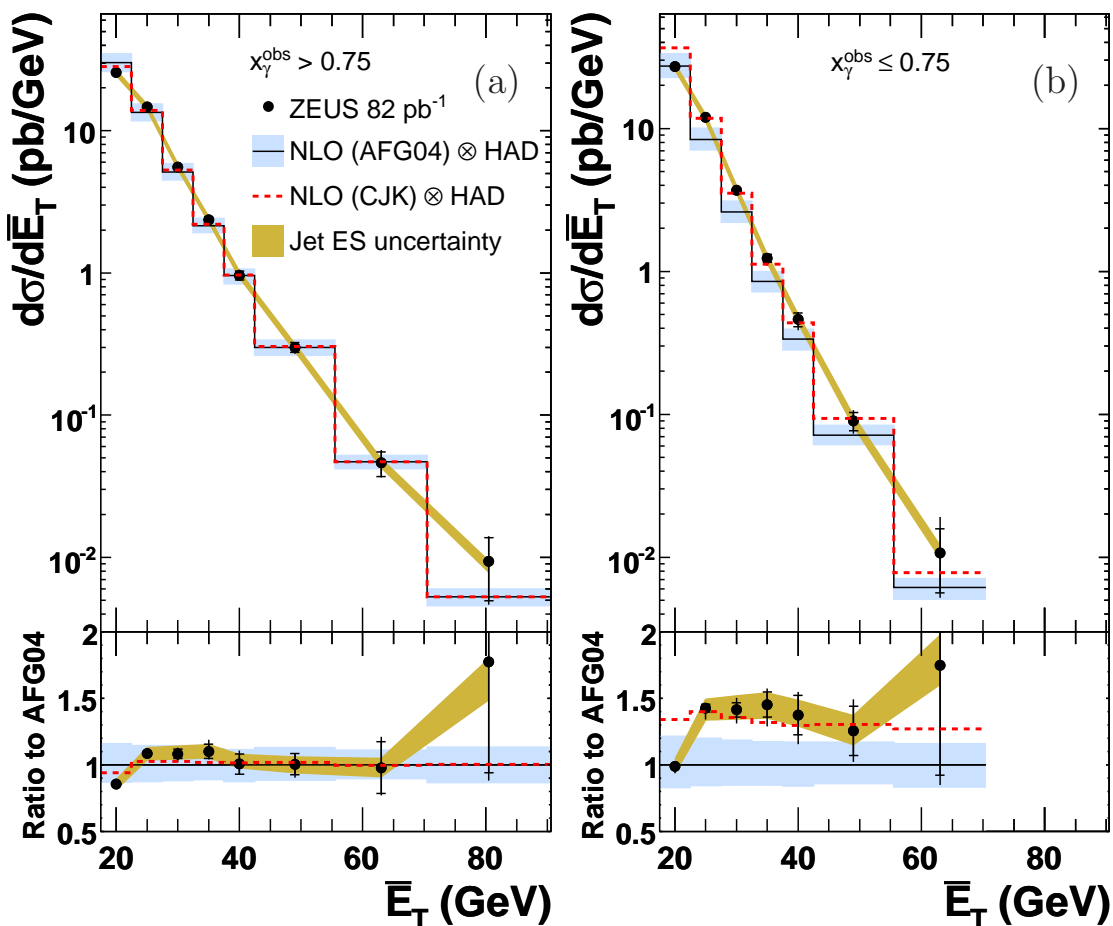


Figure 4: Measured cross-section $d\sigma/d\bar{E}_T$ for (a) $x_\gamma^{\text{obs}} > 0.75$ and (b) $x_\gamma^{\text{obs}} \leq 0.75$ compared with NLO QCD predictions using the AFG04 (solid line) and CJK (dashed line) photon PDFs. The data (dots) are shown with statistical (inner bars) and statistical and systematic uncertainties added in quadrature (outer bars) along with the jet energy-scale (Jet ES) uncertainty (shaded band). The NLO QCD predictions are shown (NLO QCD \otimes HAD) multiplied by the hadronization corrections, C_{had} , discussed in Section 5. The predictions using AFG04 are also shown with their associated uncertainties (shaded histogram) as discussed in Section 5. The ratios to the prediction using the AFG04 photon PDF are shown at the bottom of the figure.

ZEUS

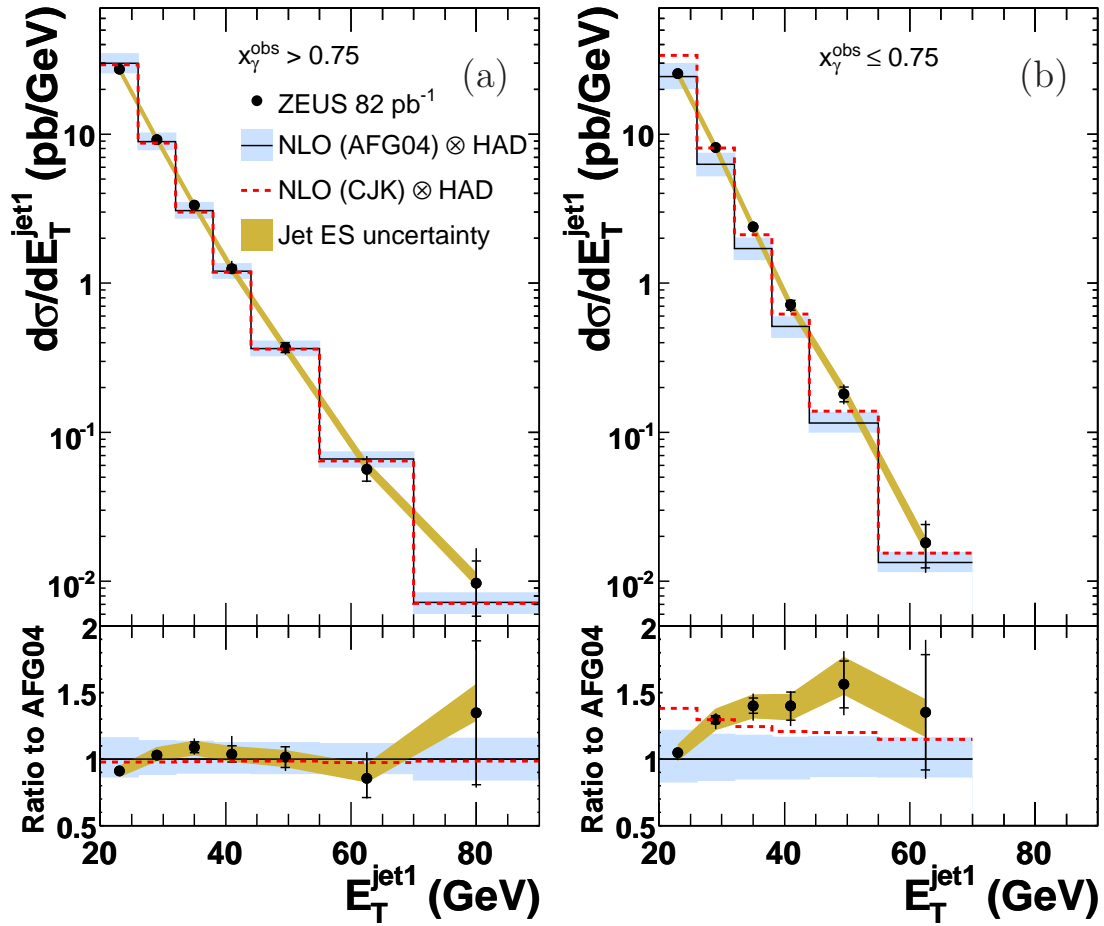


Figure 5: Measured cross-section $d\sigma/dE_T^{\text{jet1}}$ for (a) $x_\gamma^{\text{obs}} > 0.75$ and (b) $x_\gamma^{\text{obs}} \leq 0.75$. For further details, see the caption to Fig. 4.

ZEUS

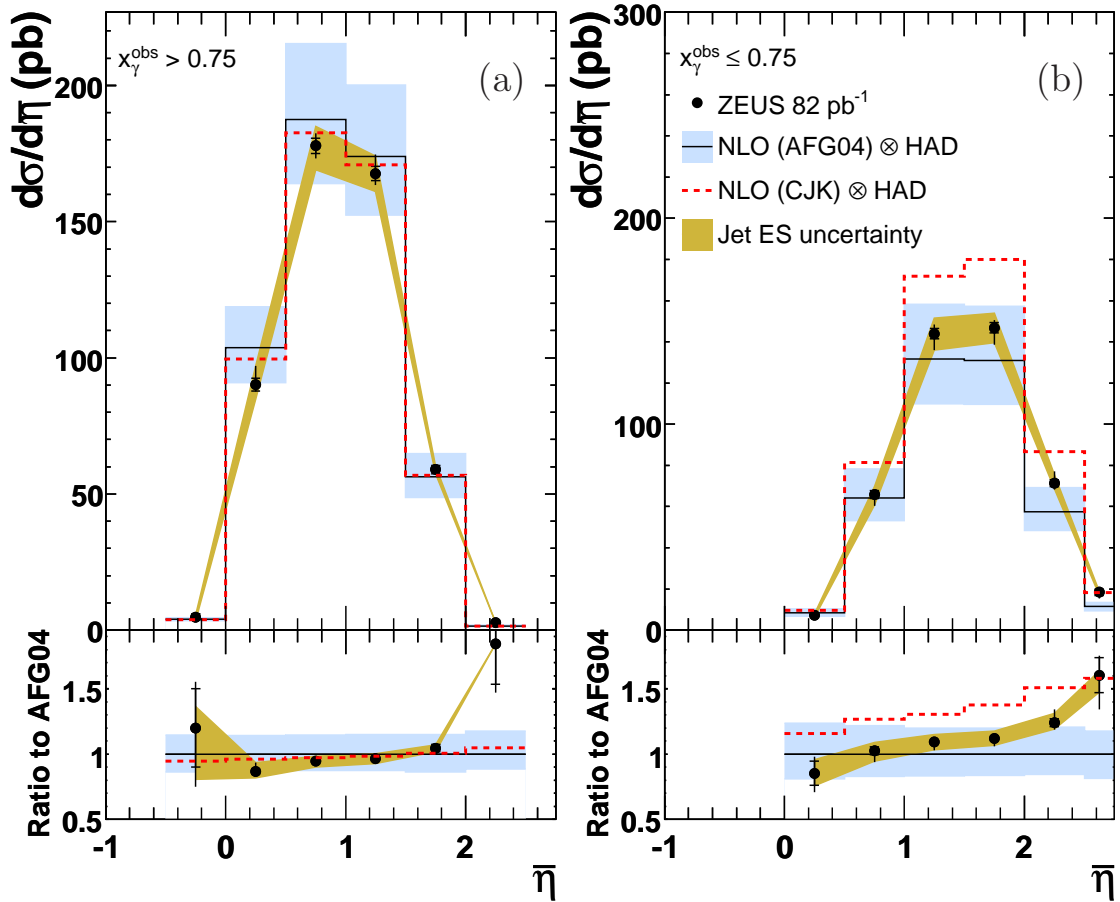


Figure 6: Measured cross-section $d\sigma/d\bar{\eta}$ for (a) $x_\gamma^{\text{obs}} > 0.75$ and (b) $x_\gamma^{\text{obs}} \leq 0.75$. For further details, see the caption to Fig. 4.

ZEUS

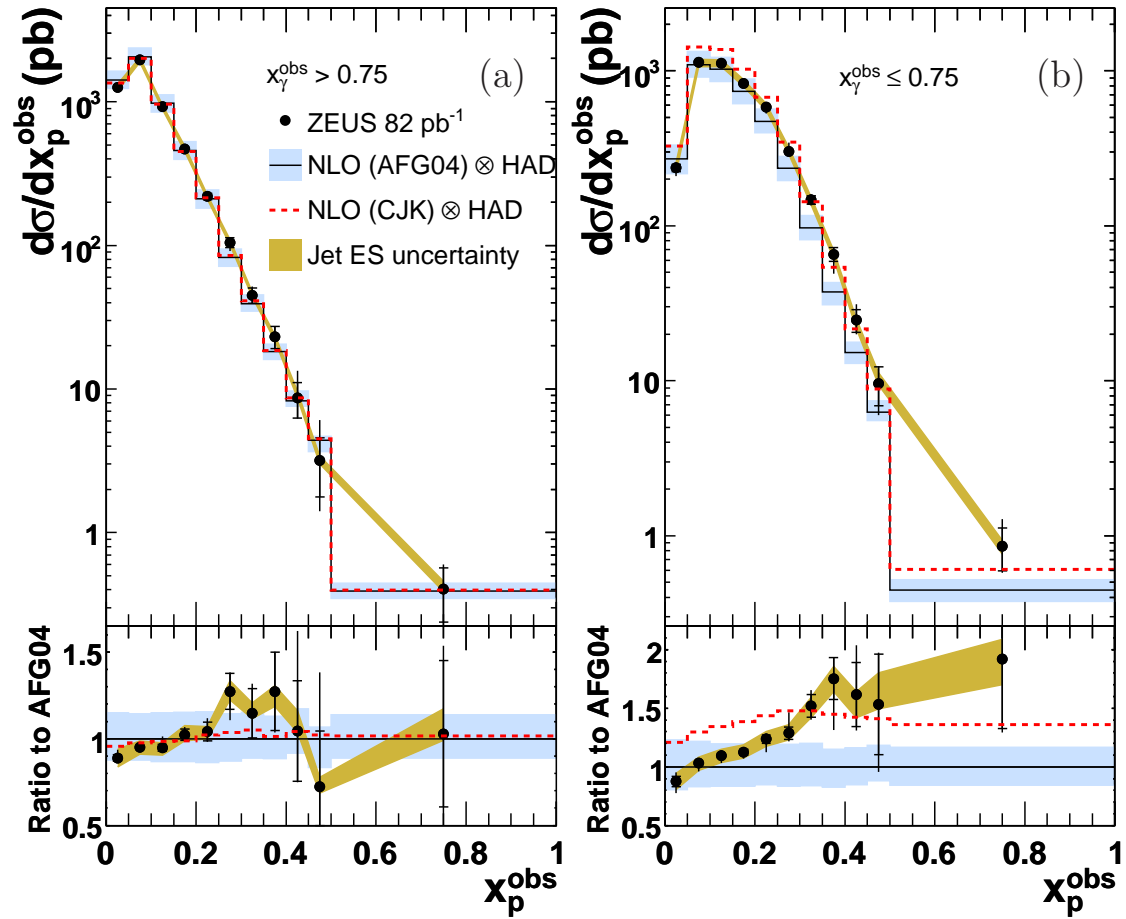


Figure 7: Measured cross-section $d\sigma/dx_p^{\text{obs}}$ for (a) $x_\gamma^{\text{obs}} > 0.75$ and (b) $x_\gamma^{\text{obs}} \leq 0.75$. For further details, see the caption to Fig. 4.

ZEUS

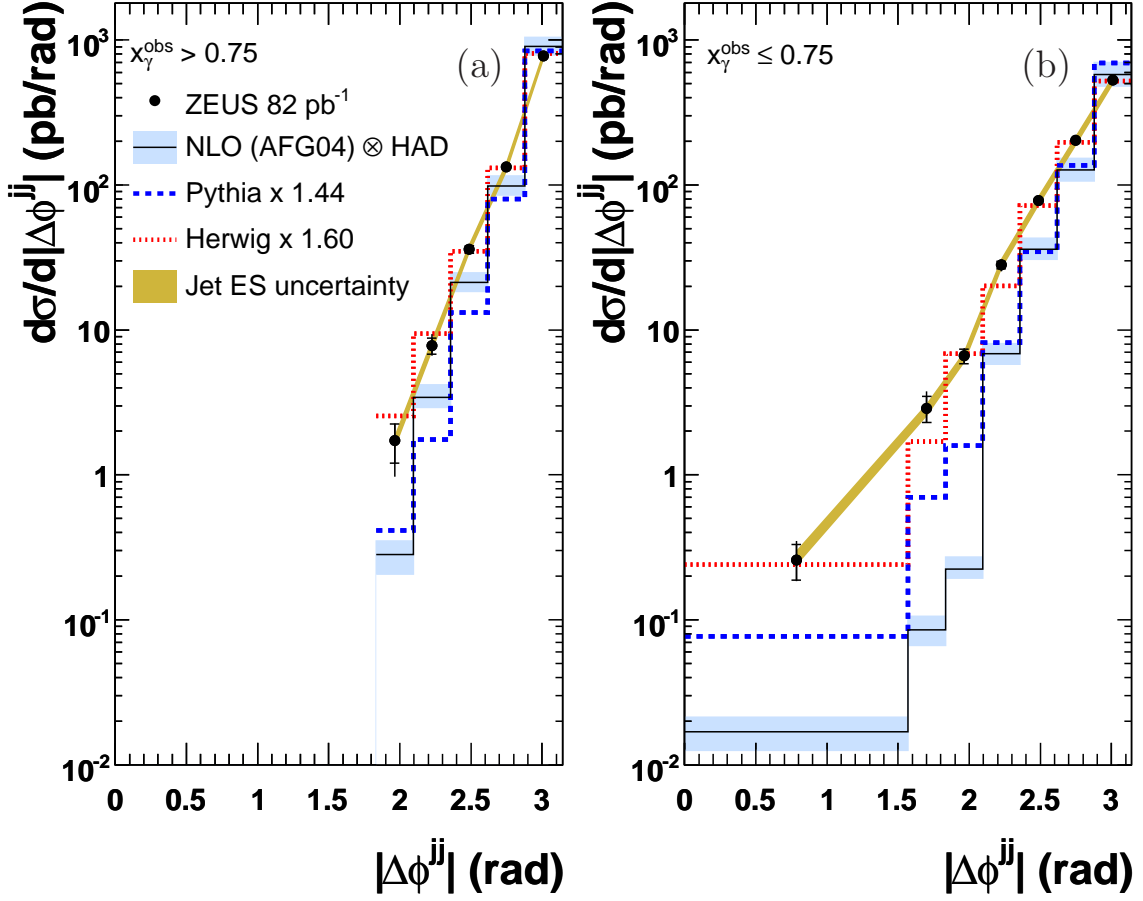


Figure 8: Measured cross-section $d\sigma/d\Delta|\phi^{jj}|$ for (a) $x_\gamma^{\text{obs}} > 0.75$ and (b) $x_\gamma^{\text{obs}} \leq 0.75$ compared with NLO QCD predictions using the AFG04 (solid line) photon PDF. Predictions from the MC programs HERWIG (dot-dashed) and PYTHIA (dashed), area normalized to the data by the factors given, are also shown. The data (dots) are shown with statistical (inner bars) and statistical and systematic uncertainties added in quadrature (outer bars) along with the jet energy-scale (Jet ES) uncertainty (shaded band). The NLO QCD predictions are shown (NLO QCD \otimes HAD) multiplied by the hadronization corrections, C_{had} , discussed in Section 5. The predictions using AFG04 are also shown with their associated uncertainties (shaded histogram) as discussed in Section 5.

ZEUS

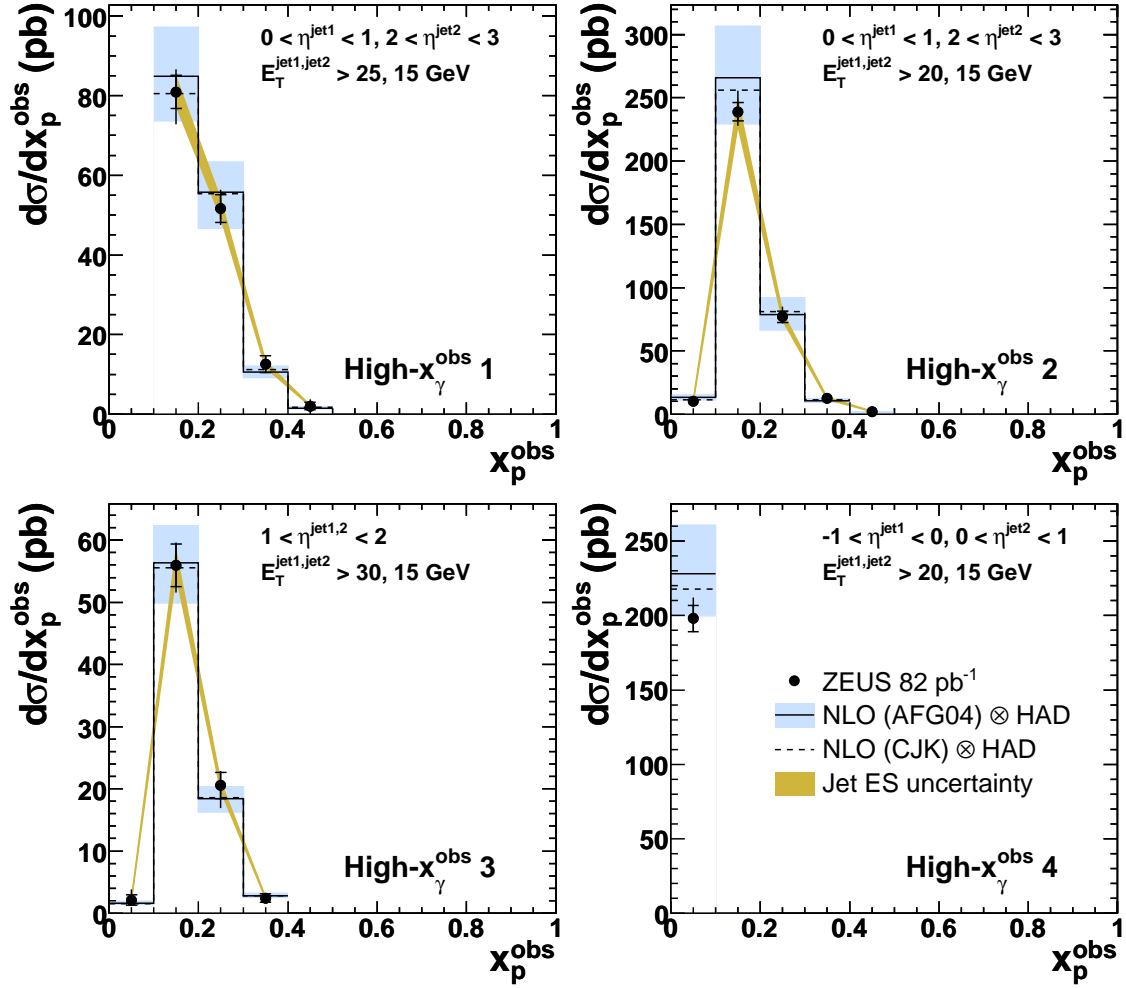


Figure 9: Optimized cross-sections $d\sigma/dx_p^{\text{obs}}$ for $x_\gamma^{\text{obs}} > 0.75$ in the kinematic regions defined in Table 1. For further details, see the caption to Fig. 4.

ZEUS

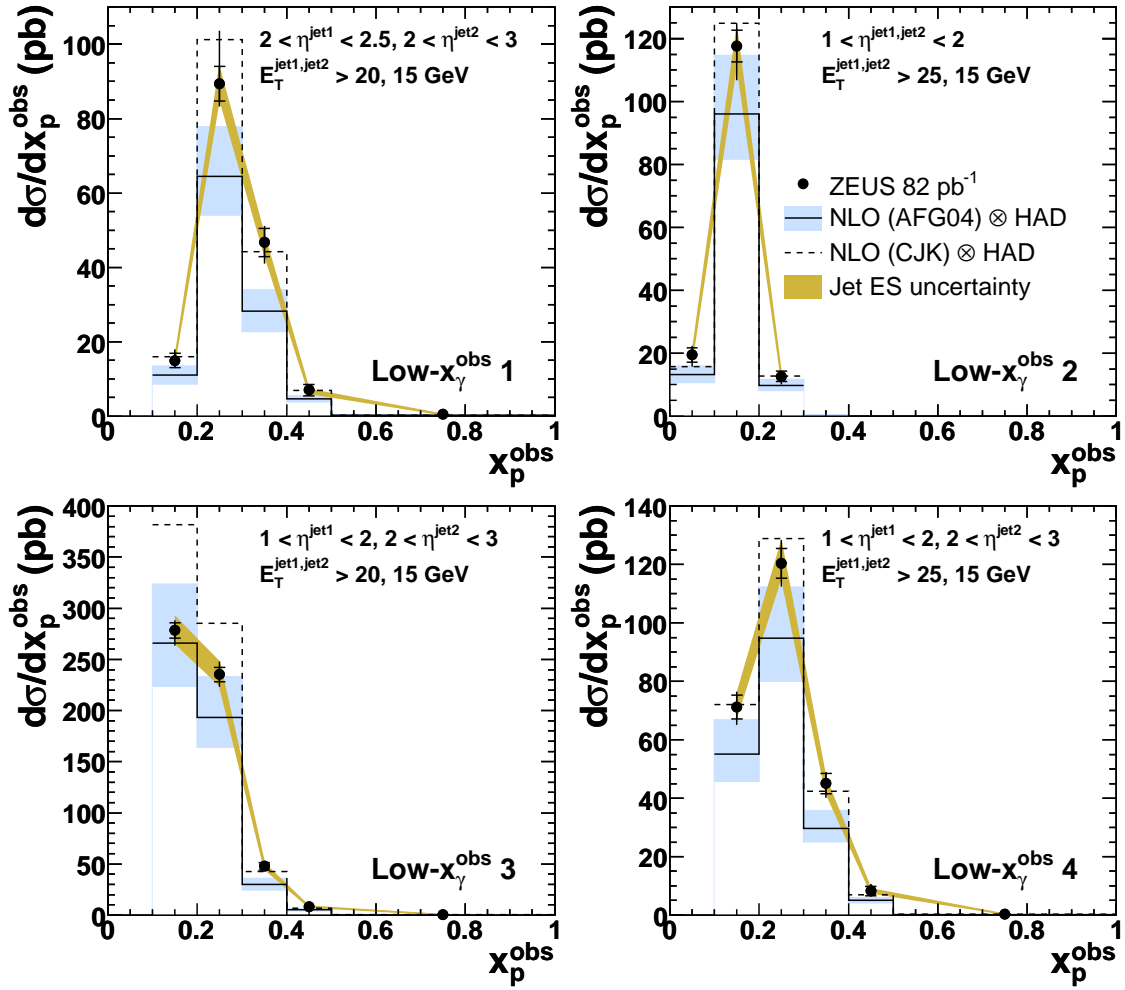


Figure 10: Optimized cross-sections $d\sigma/dx_p^{\text{obs}}$ for $x_\gamma^{\text{obs}} \leq 0.75$ in the kinematic regions defined in Table 1. For further details, see the caption to Fig. 4.

ZEUS

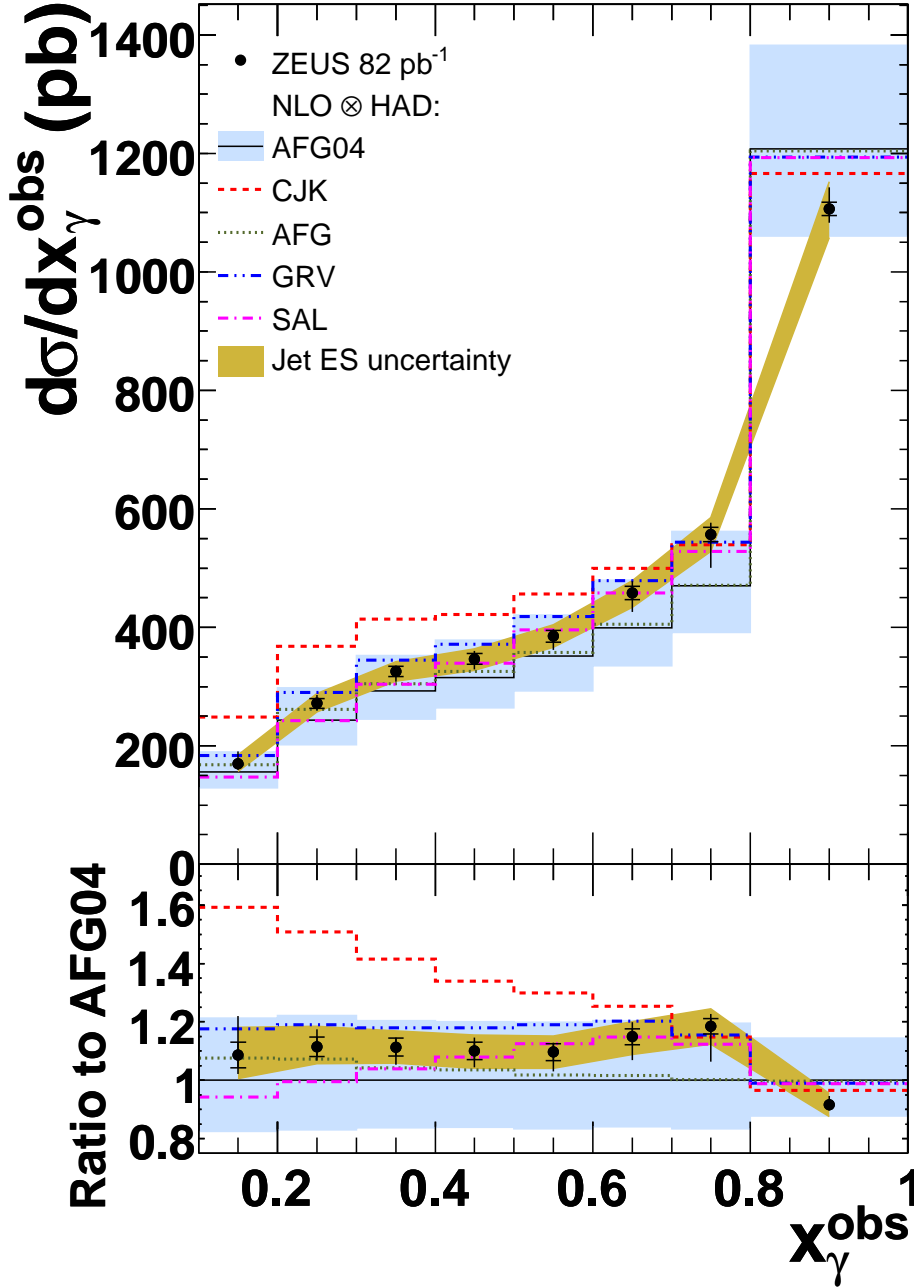


Figure 11: Measured cross-section for $d\sigma/dx_\gamma^{\text{obs}}$ compared with NLO QCD predictions using the AFG04 (solid line), CJK (dashed line), AFG (dotted line), GRV (dashed and double-dotted line) and SAL (dashed and single-dotted line) photon PDFs. The data (dots) are shown with statistical (inner bars) and statistical and systematic uncertainties added in quadrature (outer bars) along with the jet energy-scale (Jet ES) uncertainty (shaded band). The NLO QCD predictions are shown (NLO QCD \otimes HAD) multiplied by the hadronization corrections, C_{had} , discussed in Section 5. The predictions using AFG04 are also shown with their associated uncertainties (shaded histogram) as discussed in Section 5. The ratios to the prediction using the AFG04 photon PDF are shown at the bottom of the figure.

ZEUS

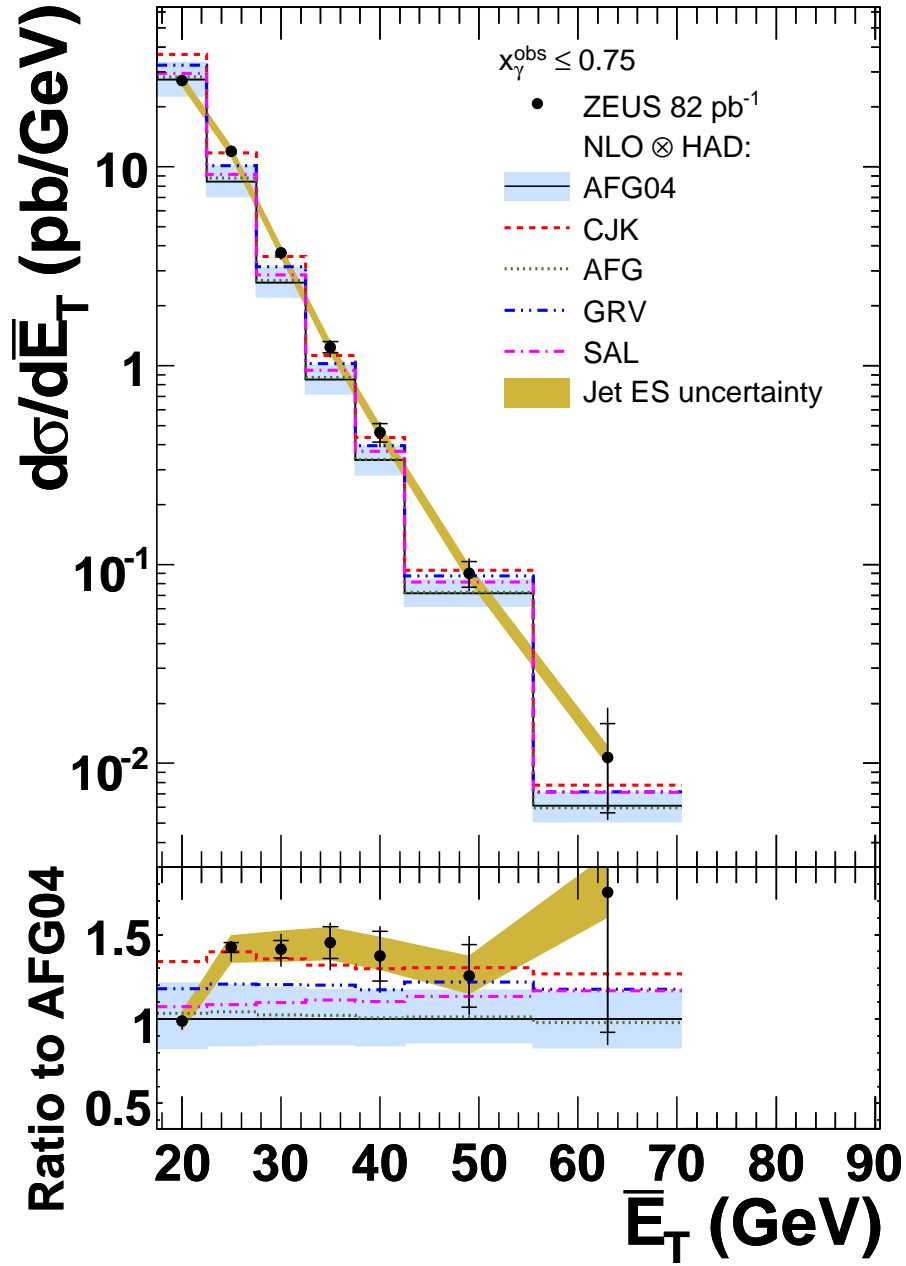


Figure 12: Measured cross-section for $d\sigma/d\bar{E}_T$ for $x_\gamma^{\text{obs}} \leq 0.75$. For further details, see the caption to Fig. 11.

ZEUS

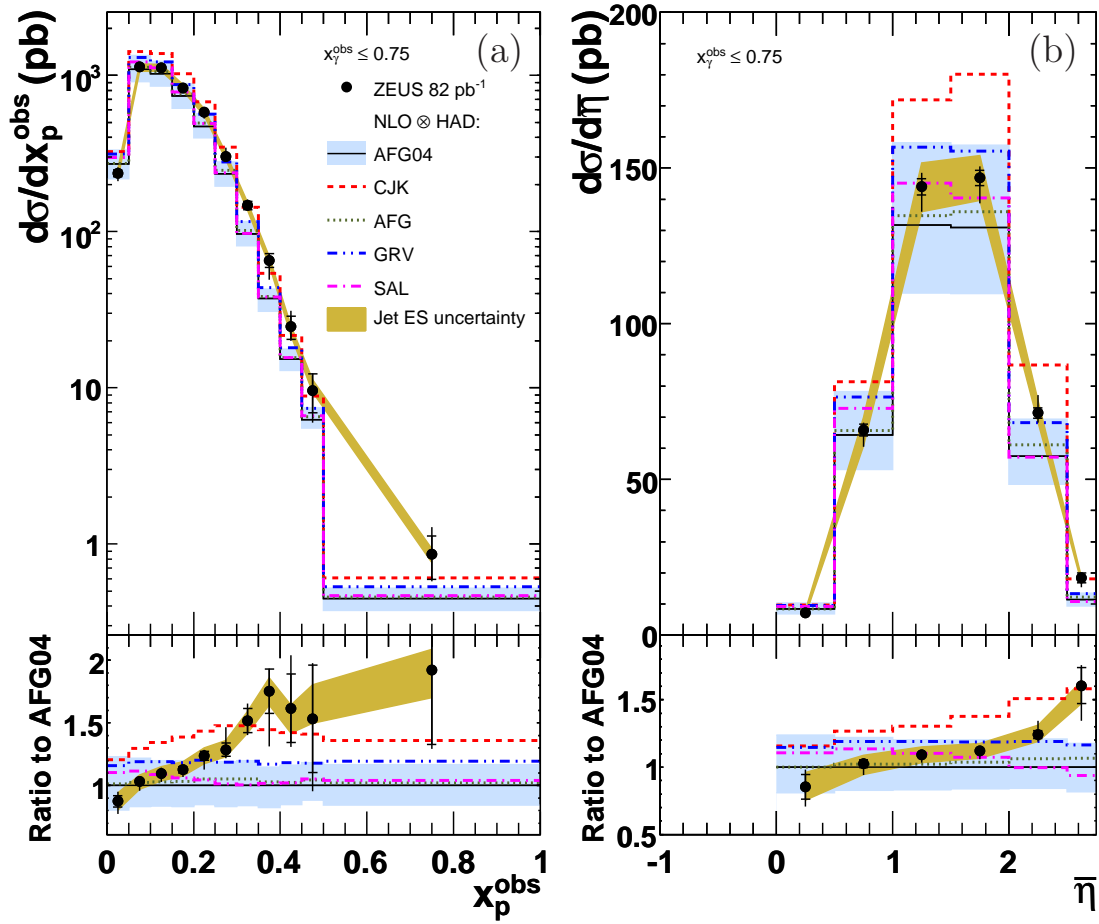


Figure 13: Measured cross-section for (a) $d\sigma/dx_p^{\text{obs}}$ and (b) $d\sigma/d\bar{\eta}$ both for $x_\gamma^{\text{obs}} \leq 0.75$. For further details, see the caption to Fig. 11.